PNAS RESEARCH ARTICLE | BIOPHYSICS AND COMPUTATIONAL BIOLOGY

Friction patterns guide actin network contraction

Alexandra Colin[a,1], Magali Orhant-Prioux[a,1], Christophe Guérin[a,1], Mariya Savinov[b,1], Wenxiang Cao[c], Benoit Vianay[d], Ilaria Scarfone[a], Aurélien Roux[e], Enrique M. De La Cruz[c], Alex Mogilner[b], Manuel Théry[a,d,2], and Laurent Blanchoin[a,d,2]

Edited by Gijsje H. Koenderink, Technische Universiteit Delft, Delft, Netherlands; received January 12, 2023; accepted August 9, 2023 by Editorial Board Member Yale E. Goldman

The shape of cells is the outcome of the balance of inner forces produced by the actomyosin network and the resistive forces produced by cell adhesion to their environment. The specific contributions of contractile, anchoring and friction forces to network deformation rate and orientation are difficult to disentangle in living cells where they influence each other. Here, we reconstituted contractile actomyosin networks in vitro to study specifically the role of the friction forces between the network and its anchoring substrate. To modulate the magnitude and spatial distribution of friction forces, we used glass or lipids surface micropatterning to control the initial shape of the network. We adapted the concentration of Nucleating Promoting Factor on each surface to induce the assembly of actin networks of similar densities and compare the deformation of the network toward the centroid of the pattern shape upon myosin-induced contraction. We found that actin network deformation was faster and more coordinated on lipid bilayers than on glass, showing the resistance of friction to network contraction. To further study the role of the spatial distribution of these friction forces, we designed heterogeneous micropatterns made of glass and lipids. The deformation upon contraction was no longer symmetric but biased toward the region of higher friction. Furthermore, we showed that the pattern of friction could robustly drive network contraction and dominate the contribution of asymmetric distributions of myosins. Therefore, we demonstrate that during contraction, both the active and resistive forces are essential to direct the actin network deformation.

cytoskeleton | contraction | friction | actin

Significance

Cell shape changes are controlled by complex sets of mechanical forces of various origins. Numerous studies have been dedicated to the role of active forces, originating from molecular motors and filament polymerization, but much less is known about the guiding role of resistive forces. Here, we show that a nonuniform distribution of friction forces between a contracting actomyosin network and its underlying substrate can direct its deformation as it contracts. Our results suggest that the contribution of resistive forces, such as viscous forces along the cell surface, can be as significant as those of active forces in driving network deformation and should be considered in mechanical models describing the regulation of cell shape and movement.

Actin and myosins are found in all eukaryotes (1–3). Myosins cross-link actin filaments, slide them along each other, and thus power large-scale network contraction (4, 5). The regulation of actomyosin contraction controls cells' shape and the mechanical forces they produce on their environment (6–8). In particular, the asymmetry of contraction directs cell deformation and orient tissue morphogenesis (9). Network deformation results from the balance between active contraction and passive resistance. The active contraction depends on the architecture of the actin network and on the amount and spatial distribution of myosins in the network (7, 10). The passive resistance is produced by network anchorages and the friction forces (11, 12). The balance of these four contributions set the rate and orientation of network deformation. Although numerous studies have focused on the mechanism that orients active contraction, the directing role of passive resistance has been much less studied. Can asymmetric friction direct a contractile network as a lagging paddle can guide a canoe?

The architecture of the actin network is defined by filament length, density, cross-linking, and their respective orientations. It can take the form of branched meshwork or bundles of filaments. Each of these modules has specific contractile properties (13). In cells, their relative dispositions form structural patterns that direct cell deformation and motion (14, 15). Structural anisotropies, such as local weakness induced by local network disassembly, generate the propagation and oscillation of contractile waves (16, 17), the maintenance of which directs the deformation and motion of poorly adhesive cells (18–20). Similarly, local structural reinforcement, by network polymerization in response to the optoactivation of Rac, for example, directs cell deformation in the opposite direction (21, 22).

The spatial distribution of myosins depends on their recruitment on actin filaments and activation by signaling pathways (23, 24). Their subcellular distributions generate patterns of contraction, asymmetric cell deformation, and migration (25–27). Reconstituted systems were used to show that spatial patterns of myosin activation determine the shape and boundaries of the contracting region of the network (10). In adherent cells, the actin retrograde flow accumulates myosins at the rear of the lamella where they form a subcellular pattern of contractile bundles propelling cells (20, 28–30) and neuronal growth cones (31). In poorly

Author contributions: A.C., M.O.-P., C.G., M.S., B.V., A.R., E.M.D.L.C., A.M., M.T., and L.B. designed research; A.C., M.O.-P., C.G., M.S., I.S., and A.M. performed research; E.M.D.L.C. contributed new reagents/analytic tools; A.C., M.O.-P., C.G., M.S., W.C., B.V., A.M., and M.T. analyzed data; and A.C., E.M.D.L.C., A.M., M.T., and L.B. wrote the paper.

The authors declare no competing interest.

This article is a PNAS Direct Submission. G.H.K. is a guest editor invited by the Editorial Board.

[1]A.C., M.O.-P., C.G., and M.S. contributed equally to this work.

[2]To whom correspondence may be addressed. Email: manuel.thery@cea.fr or laurent.blanchoin@cea.fr.

This article contains supporting information online at https://www.pnas.org/lookup/suppl/doi:10.1073/pnas.2300416120/-/DCSupplemental.

Published September 19, 2023.

adhesive cells, a global increase of cell contraction triggers a wave that concentrates myosin in the back and propels cell motion forward (32, 33). Reversal of this contraction pattern is necessary when immune cells reverse their polarity to process the antigens they encounter in the front (34). Subcellular activation patterns of myosins could also be induced with optogenetic tool to induce local contraction and asymmetric deformation contributing to cell motion (20, 35–37). At larger scales, in tissues, asymmetric localization or gradients of myosins power anisotropic tissue deformation (38–41).

The anchorages link the actin network to the extracellular matrix or to surrounding cells via integrins or cadherins (9). In the local absence of anchorages in the plasma membrane, cortical actin filaments can glide and coalesce to form contractile bundles that concentrate forces (42, 43). By contrast, filaments have limited translocation freedom in regions where anchorages are present, so they assemble thinner and pinpointed bundles (42, 44). Thus, extracellular patterns of adhesion are converted into a pattern of structure (45) and a pattern of forces (46). As a consequence, cells tend to detach from regions of lower adhesiveness and move toward regions of higher adhesiveness (47, 48). Such polarization of actomyosin network deformation can be externally induced by inducing a local detachment of the cell, which is sufficient to induce cell motion toward the opposite direction (49).

Friction forces resist the relative sliding of the actin network along its anchoring surface (50, 51) and thereby allow cell translocation (52, 53). They also limit the sliding of actin filaments along each other and thus control network deformation and rearrangements as it contracts (36, 54). In tissues, friction has been proposed to limit the instabilities and direct the self-organization of contractile waves into regular banding patterns (55). This process of directed contraction, in principle, orients network contraction toward regions of higher friction. Although the global role of friction forces has been clearly identified in the migration of poorly or nonadhesive cells (56, 57), or in the motion of encapsulated cell extracts (58), it is still unclear whether the pattern of friction can orient cell and tissue deformation. Single cells and cellular aggregates move toward less deformable regions where friction forces between the contracting actin network and the substrate are higher (59–61). At larger scales, the anisotropic pattern of friction has been proposed to account for the directed contraction of *Drosophila* apical surface during gastrulation (62), the morphogenesis of the neurectoderm in zebrafish embryos (63), and the emergence of chiral flows in the cortex of *Caenorhabditis elegans* embryos (64). However, in cells, and a fortiori in tissues, it is challenging to distinguish the effect of the friction pattern from those of structure, myosin, and adhesion patterns. These parameters influence each other and self-organize together (26, 30, 31, 65). Testing the specific role of friction pattern requires to modulate the spatial distribution of friction while all other contributions, structure, myosin, and anchorage, are homogeneous. Here, we used geometrically controlled reconstituted actomyosin networks (66), contracting either on glass or on lipid-coated surfaces (51, 67, 68), to investigate the specific role of friction in the guidance of large-scale contractions.

Results

Actin Assembly Rates Are Distinct on Glass and Lipid Micropatterns. To study the role of friction on the contraction of actomyosin networks, we used surface micropatterning to control the initial shape of the network. Our protocol to micropattern actin networks on supported lipid bilayer was inspired from several preceding methods. In brief, glass coverslips coated with a Polyethylene glycol (PEG) layer were exposed to deep Ultraviolet (UV) through a photomask in order to remove the PEG locally (69). The coverslips were then immersed in a solution containing small unilamellar vesicles (SUVs), containing 0.25% of lipids conjugated with biotin. The vesicles exploded and spread in contact with the regions presenting bare glass (70). A Nucleation Promoting Factor (NPF; Snap-Streptavidin-WA-His) was then attached to these patterned lipids via a biotin–streptavidin link. The actin polymerization mix was then added onto this micropatterned surface to generate actin networks of controlled geometries (66) (Fig. 1*A*).

We first checked that NPF was active in our conditions and could induce the assembly of a branched actin network on the micropatterned lipid bilayer (Fig. 1*B* and Movie S1), as previously shown on infinite bilayers (71, 72). We also confirmed that lipids and NPF could diffuse freely at normal rates (73, 74) before and after actin polymerization despite the immobility of the dense actin mesh (Fig. 1*C*, *SI Appendix*, Fig. S1, and Movie S2). Interestingly, we observed that the efficiency to generate an actin assembly with NPF grafted onto a lipid micropattern was an order of magnitude higher (10 times faster) than that of NPF grafted onto a glass micropattern (Fig. 1 *D* and *E* and Movie S3). Considering that network density limits network contraction (72, 75), we determined the concentrations of NPF that induced similar actin network assembly on the glass and lipid micropattern (Fig. 1 *D* and *E* and Movie S3) to investigate specifically the role of substrate friction on network contraction. Hence, in the following experiments, the concentration of NPF will be 1 μM on glass and 1 nM on lipids.

Friction Slows Down Network Deformation upon Contraction. In the following experiments, friction could arise from either 1) attachment between the actin network and the NPF or 2) nonspecific interactions between actin filaments and the surface. We rule out the first possibility for the following reasons: We monitored the initial events of branch formation and quantified that filament diffusion was the same before and after branch formation (*SI Appendix*, Fig. S2 *A* and *B*), demonstrating that the NPF does not remain attached to the actin network, confirming existing results in the literature (76). We investigated next the possibility that friction is due to the nonspecific interaction between actin filaments and the surface (glass or lipids). Therefore, we followed the diffusive movement of individual actin filaments on NPF micropatterns on a lipid or glass surface. We tracked using TIRF (total internal reflection fluorescence) microscopy the center of mass of these filaments and evaluated their translational diffusion coefficient from the Mean Square Displacement (MSD) analysis. We measured that the diffusion coefficient on glass patterns is slower than on lipid patterns, demonstrating that individual actin filaments experience greater friction when they come into contact with a glass surface than with a lipid surface (*SI Appendix*, Fig. S2 *D–F*). Moreover, when an additional blocking step with Bovine serum albumin (BSA) is performed on the NPF-coated glass surface, we found that the diffusion coefficient of actin filaments becomes similar to that of the lipid surface. This demonstrates that the contribution of NPF–actin interaction to the friction is limited (*SI Appendix*). We also tracked branches at the early stages of their formation and measured their diffusion coefficient from the MSD. Similarly, we found that branches diffuse slower on glass than on lipid micropattern, showing that they experience a higher friction (*SI Appendix*, Fig. S2 *C* and *F*). Einstein relation then allows us to conclude that the actin–glass friction is roughly three-fold greater than the actin–lipid friction (*SI Appendix*).

We then assessed the impact of the friction between the actin filaments and the underlying substrate during the actomyosin network contraction. Addition of a double-headed [heavy-meromyosin

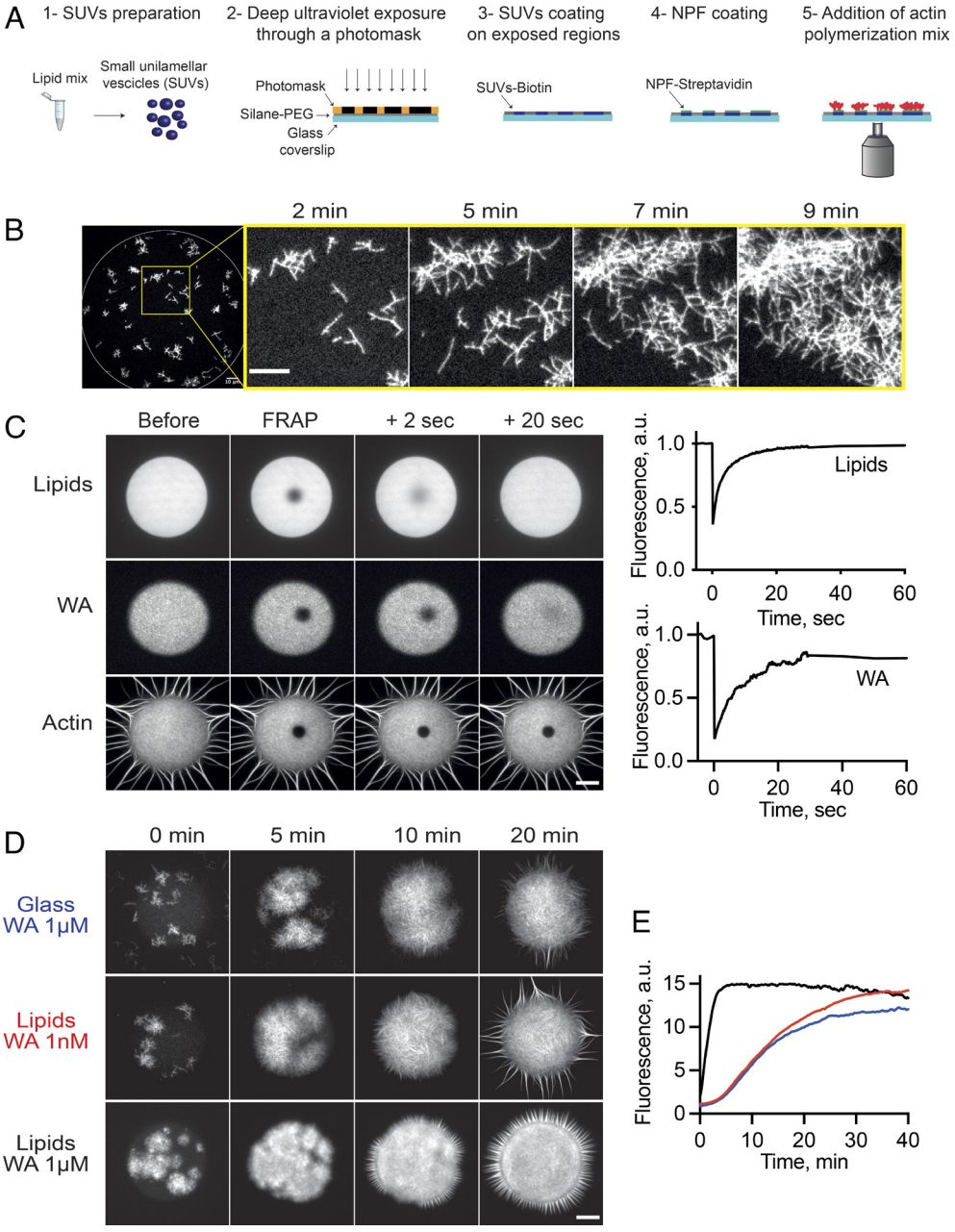

Fig. 1. Actin assembly on glass or lipid micropatterns. (*A*) Cartoon of the method to constrain branched actin network assembly on glass or lipid micropatterns. (*B*) TIRF imaging of branched actin assembly on lipid micropattern (disk, diameter 135 μm). Biochemical conditions: WA 1 nM, Actin 1 μM, Human Profilin 3 μM, Arp2/3 complex 25 nM. (Scale bar: 10 μm.) (*C*) Characterization of the diffusion property of the lipid micropattern. *Left*: TIRF imaging before and after FRAP (zone diameter: 10 μm) on lipids, NPF (WA), and Actin (after network polymerization). Biochemical conditions: disk micropattern (diameter 68 μm), WA 1 nM, Actin 1 μM, Human Profilin 3 μM, and Arp2/3 complex 25 nM. (The scale bar is 20 μm.) *Right*: Fluorescence measurements from the images on the left demonstrate that the lipids and the NPF diffuse freely in our experimental conditions. (*D*) Comparison of the efficiency of actin network growth on lipid versus glass micropatterns. TIRF imaging of branched actin assembly on lipid and glass disk micropatterns (diameter 68 μm). Biochemical conditions: NPF concentration is indicated on the figure. Actin 1 μM, Human Profilin 3 μM, and Arp2/3 complex 25 nM. (The scale bar is 20 μm.) (*E*) Kinetics of actin assembly on lipid versus glass micropattern.

(HMM)-like] myosin VI (13, 75) to a disk- or a square-shaped network on glass or lipid induced its contraction toward the center of the initial shape (Fig. 2 *A* and *B* and Movies S4 and S5).

The contraction process followed three phases (described in ref. 13) and illustrated by the variation of the area covered by the actin network over time (Fig. 2). An a) initial growth phase corresponding to the assembly of actin filaments in the first 10 min after the addition of actin monomer to the reaction mixture; b) a lag, corresponding to the loading of myosins on the actin filaments (*SI Appendix*, Fig. S4 *A–C*) and their local reorganization without any global deformation of the entire network; and c) the deformation by contraction of the network toward the center of the micropattern (Fig. 2 *C* and *D*). The initial delay of assembly was identical for lipid (red curve) or glass (blue curve) on disks and squares (Fig. 2 *C* and *D*). However, the lag and deformation phases were different on glass and lipids. The lag phase was shorter, and the deformation rate was faster on lipids than on glass (Fig. 2 *E* and *F*). Similar observations were made for the contraction of networks on rectangles of identical area (*SI Appendix*, Fig. S3). This showed that the lower friction on lipids than on glass facilitates actin network contraction by myosins. In addition, we also looked

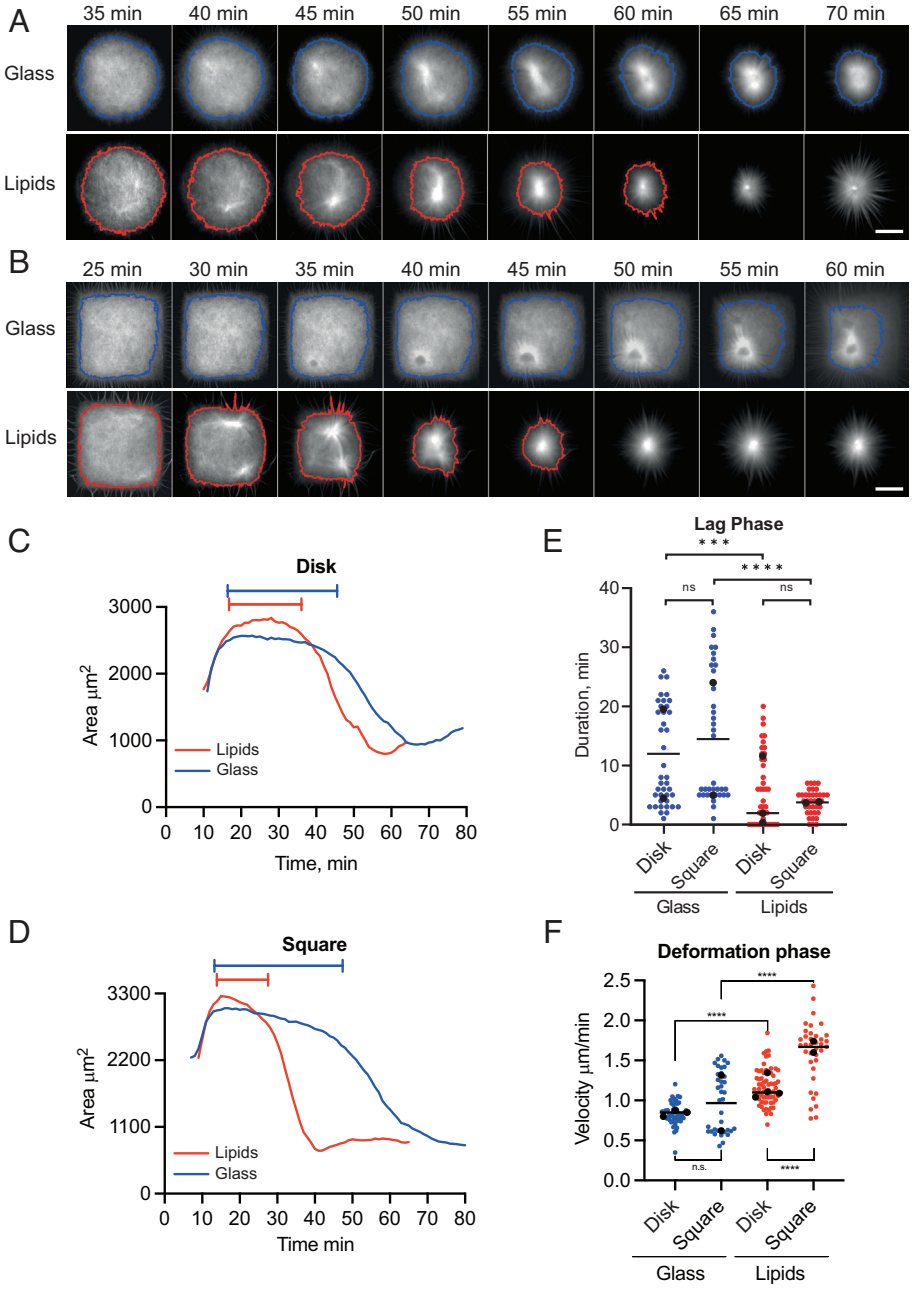

Fig. 2. NPF attachment conditions control actin network contractile response. (*A*) Kinetics of contraction of a disk-shaped actin network on glass or lipid micropattern. Time-lapse imaging of actin network contraction on a glass or lipid disk (diameter 68 µm) micropattern. The line (blue for glass; red for lipids) corresponds to the contours of the actin network (*Materials and Methods*). Biochemical conditions: On glass micropattern, WA = 1 µM; on lipid micropattern: WA = 1 nM. Actin 1 µM, Human Profilin 3 µM, Arp2/3 complex 25 nM, and Myosin VI 14 nM. (The scale bar is 20 µm.) (*B*) Kinetics of contraction of a square-shaped actin network on glass or lipid micropattern. Time-lapse imaging of actin network contraction on a glass or lipid square (length 60 µm) micropattern. The line (blue for glass; red for lipids) corresponds to the contours of the actin network (*Materials and Methods*). Biochemical conditions: On glass micropattern, WA = 1 µM; on lipid micropattern: WA = 1 nM. Actin 1 µM, Human Profilin 3 µM, Arp2/3 complex 25 nM, and Myosin VI 14 nM. (The scale bar is 20 µm.) (*C* and *D*) Measured actin area as a function of time for the lipid (red) or glass (red) conditions on disk (*C*) or square (*D*) micropattern. The period defined at the top of the graph determines the lag phase for each condition. (*E*) Duration of the lag phase preceding the contraction for the lipid or glass conditions on disk or square micropattern. Data are represented with a superplot. Disk glass: n = 40; N = 2; *median* = 7.5. Disk lipids n = 41; N = 3; *median* = 4.0. Square glass n = 37; N = 2; *median* = 7.0. Square lipids n = 37; N = 2; *median* = 4.0. Mann–Whitney statistics: disk glass/disk lipids *P* value = 0.0010***, square glass/square lipids *P* value ≤ 0.0001****, disk glass/square glass *P* value = 0.1247 ns, and disk lipids/square lipids *P* value = 0.5360 ns. (*F*) Velocity of the phase contraction phase for the lipid or glass conditions on disk or square micropattern. Data are represented with a superplot. Disk glass n = 53; N = 3; *median* = 0.8346, disk lipids n = 68; N = 4; *median* = 1.133, square glass n = 37; N=2; *median* = 1.013, and square lipids n = 37; N = 2; *median* = 1.694. Mann–Whitney statistics: disk glass/disk lipids *P* value ≤ 0.0001****, square glass/square lipids *P* value ≤ 0.0001****, disk glass/square glass *P* value = 0.2761 ns, and disk lipids/square lipids *P* value ≤ 0.0001****.

at the myosin signal at the beginning of the contraction and correlated it with the contraction velocity (*SI Appendix*, Fig. S4 *D–F*). Assuming that the contractile force is proportional to the myosin concentration and the velocity is equal to the ratio of the force and the friction coefficient, the slope of the myosin concentration–velocity relation is inversely proportional to the friction coefficient. Thus, the ratio of the slopes for glass and lipid conditions gives the ratio between the two respective frictions. The data reported in *SI Appendix*, Fig. S4*F* indeed show that a slower velocity is generated on glass, compared to that on lipid, for the same myosin concentration, and gives the ratio of 3 between the respective slopes, confirming the independent

friction estimates made by measuring diffusion and using Einstein relation (*SI Appendix*, Fig. S2).

Friction Limits Large-Scale Coordination of Network Contraction. During this study, we noticed that network deformation seemed more uniform and coordinated on lipids than on glass. To characterize this, we photobleached a grid in the network and monitored its deformation during the contraction process. We found that on glass, local regions could initiate their deformation independently, while on lipids, the deformed regions formed a continuum and contracted together across the network (Fig. 3*A* and *SI Appendix*, Fig. S5). To further quantify this, we tracked actin network deformation by particle image velocimetry (Fig. 3 *B* and *C*). For the analysis, we decomposed the square in four quadrants and summed the velocities of the moving parts in each quadrant. Measurements showed that the deformation of the four quadrants was not similar nor synchronized on glass, but they were precisely coordinated on lipids (Fig. 3 *B* and *C* and *SI Appendix*, Fig. S6). Interestingly, this difference of spatial and temporal coordination during contraction had an impact on the position of the point of convergence of the contraction process, which was closest to the center of the initial shape on lipids than on glass (Fig. 3*D* and Movies S6 and S7). This showed that the lower friction on lipids than on glass allowed a more integrated and coordinated actomyosin contraction.

A Pattern of Friction Can Guide Network Contraction. The abovementioned effect of friction on the rate and coordination of the contraction process suggested that heterogeneity in the friction coefficient between the actin network and the underlying substrate might direct network contraction. To test this hypothesis, we developed a method to generate a heterogeneous friction pattern below uniform and geometrically controlled actin networks (*SI Appendix*, Fig. S7*A*). We used a digital micromirror device (DMD) to photoactivate distinct regions sequentially and coat them with distinct components (*Materials and Methods* and *SI Appendix*, Fig. S7*A*). On a PEG layer, we generated disks, squares, or rectangles, half of which was made of bare glass coated with 1 μM NPF, and the other half was coated with lipids and 1 nM NPF to obtain similar actin polymerization kinetics on the two halves and thus a homogeneous network over the entire micropattern. We confirmed that lipids and WA diffused on the lipid half and not on the glass half (*SI Appendix*, Fig. S7*B*) and that the networks contracted according to the three phases described previously (*SI Appendix*, Fig. S8).

Strikingly, while networks on homogeneous disk-shape lipid micropatterns contracted precisely toward the centroid of the initial geometry, they showed a clear off-centering toward the region of higher friction on heterogeneous glass–lipid micropatterns (Fig. 4 *A* and *B* and Movies S9–S14). This deviation resulted from the faster deformation of the actomyosin network on lipids than on glass (*SI Appendix*, Fig. S8). We tested additional patterns of friction in squares and rectangles and noticed that the network compacts to a point which is biased toward the center of the higher friction region (Fig. 4 *C*–*F*). These results demonstrated that a friction pattern can guide actomyosin network deformation.

Numerical Simulations Account for the Trajectories of Myosin Spots during Network Contraction. To further understand the way actomyosin networks deform as they contract, we turned to computational modeling. We model the actomyosin network as a two-dimensional viscoelastic network with active contractile stresses generated by myosin concentrated in several foci (77). The internal (passive viscoelastic and active contractile) stresses in the network are balanced by friction between the network and substrate (glass or lipid), which we model as effective viscous drag with the drag on glass higher than that on lipid. This model is implemented as a network of nodes connected by a viscous dashpot with the substrate. Neighboring nodes are connected by the viscous dashpot and elastic (nonlinear) spring in series responsible for viscous and elastic deformations inside the network (*SI Appendix*, *Model Description* and Fig. 5*A*).

We first simulated the contraction of the network on homogeneous lipid square, with initial myosin foci appearing in four corners of the square (Fig. 5*B* and Movie S16). The simulations showed the temporal sequence of the network deformation like those observed experimentally (Fig. 2*B*). Specifically, the simulations correctly predict that the network corners get rounded right after the onset of the contraction (Fig. 5*B*). Note also that the area near the center of the network did not deform until late stage of contraction (Fig. 5*B*), which is also observed in experiments (Fig. 3*A*). We then plotted the predicted myosin foci's trajectories for homogeneous patterns. Interestingly, for the homogeneous pattern, the model predicts that regardless of the initial positions and even number of myosin spots, the spots drifted straight to the center of the square and converged to it (Fig. 5*C*). Importantly, the model predicted that to generate the observed ratio of the contractile rates on glass and lipid, the respective ratio of the friction coefficients has to be approximately 3 (*SI Appendix*), as is already established by two independent experimental estimates.

Remarkably, when a heterogeneous pattern of friction was simulated with the exact same initial myosin distribution, the final point of contraction was shifted toward the side of high friction as observed on the experimental data (Fig. 5*D* and Movie S17). Furthermore, for the square homogeneous or heterogeneous patterns, we found that regardless of the initial position and number of myosin foci, the foci drifted straight to the center of the friction pattern and then converged to it (Fig. 5 *C* and *D* and see *SI Appendix*, Fig. S9 *A* and *B* for examples with different positions of myosin foci). This is reminiscent of the ballistic contractility previously described (77). Finally, the trajectories predicted on homogeneous or heterogeneous rectangles showed myosin foci first converging to the point of intersection of the bisecting lines of the angles and then moving to their destination, defined by the distinct weights of the two friction patterns. (*SI Appendix*, Fig. S9 *C*–*F*).

Two contraction features are illustrated by these trajectories. First, the global character of the contraction: myosin foci integrate large areas in the definition of their motion, which is largely the consequence of the highly interconnected character of the actomyosin network and global propagation of the internal stresses (*SI Appendix*, *Model Description*). Second, the predicted locations of the convergence points of the contracted heterogeneous pattern are largely insensitive to the initial myosin distributions (and to the number of myosin foci) but determined by the adhesion distribution.

Consequently, heterogeneity of contractility (initial myosin distribution) does not explain nor impact contraction asymmetry. Although the contraction is local and randomly initialized by myosin foci, a combination of network geometry and external friction heterogeneity leads to a robust global polarized contraction. Thus, our model proposes that the friction pattern can dominate over the initial distribution of contractility to drive contraction asymmetry.

Friction Acts as a Master Control of Symmetry of Actomyosin Meshwork Contraction. We tested the predictions of the model by analyzing the localization and trajectories of myosin foci in our experimental data. Foci formed rapidly and were randomly

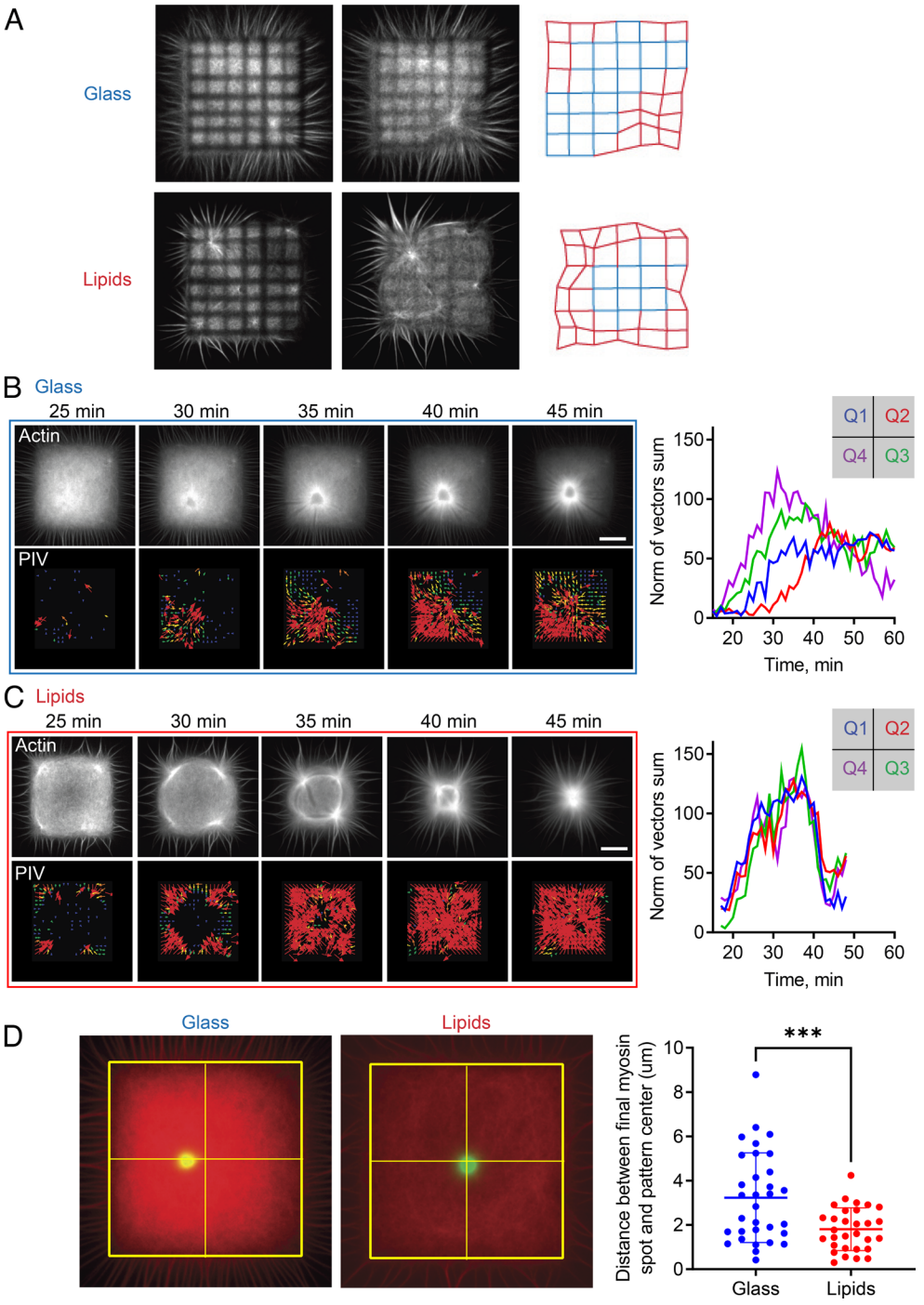

Fig. 3. Lower friction improves the coordination of the contraction process. (*A*) Local deformation of the actin network. A photobleached grid shape was performed on actin networks polymerized on glass or lipid micropatterns. Then, deformations of the actin network were followed by following the grid deformation. (*B*) *Left Top*: Example of an actin network grown on glass substrate pattern used for PIV analysis. *Left Bottom*: PIV analysis of the actin network shown above. *Right*: Resultant of vector sum for each quadrant defined on the pattern as a function of time (*Materials and Methods*). (*C*) Same as *B* with an actin network grown on lipid substrate. (*D*) *Left*: Snapshots of the final position of myosin spot for actin networks grown on glass or lipid square micropattern. *Right*: Quantification of the distance between the final myosin spot and the pattern center for networks grown on glass or lipids. N = 2 independent replicates with n = 18 and n = 12 patterns for the lipids condition and n = 19 and n = 13 patterns for the glass condition. Individual points for each pattern are represented. Mean and SD are plotted on top of the points. Unpaired *t* test: *P* value ≤ 0.001***. Biochemical conditions for Fig. 3: On glass micropattern, WA = 1 μM; on lipid micropattern: WA = 1 nM. Actin 1 μM, Human Profilin 3 μM, Arp2/3 complex 25 nM, and Myosin VI 14 nM.

distributed in networks assembled on homogeneous square lipid micropatterns (Fig. 6*A*). The heterogeneity of these initial distributions, which could be quite asymmetric, and sometimes even made of a single and off-centered focus, did not impact the position of the convergence point, at the square center, nor the trajectories, which were directed straight toward it (Fig. 6*A* and Movie S10). These observations were consistent with the model (Fig. 5 *B* and *C*) and demonstrate that the actomyosin network contraction integrates the entire shape of the network independently of the asymmetry of myosins distribution.

Tracking myosin foci on homogeneous rectangular lipid micropatterns confirmed the above conclusions on the absence of

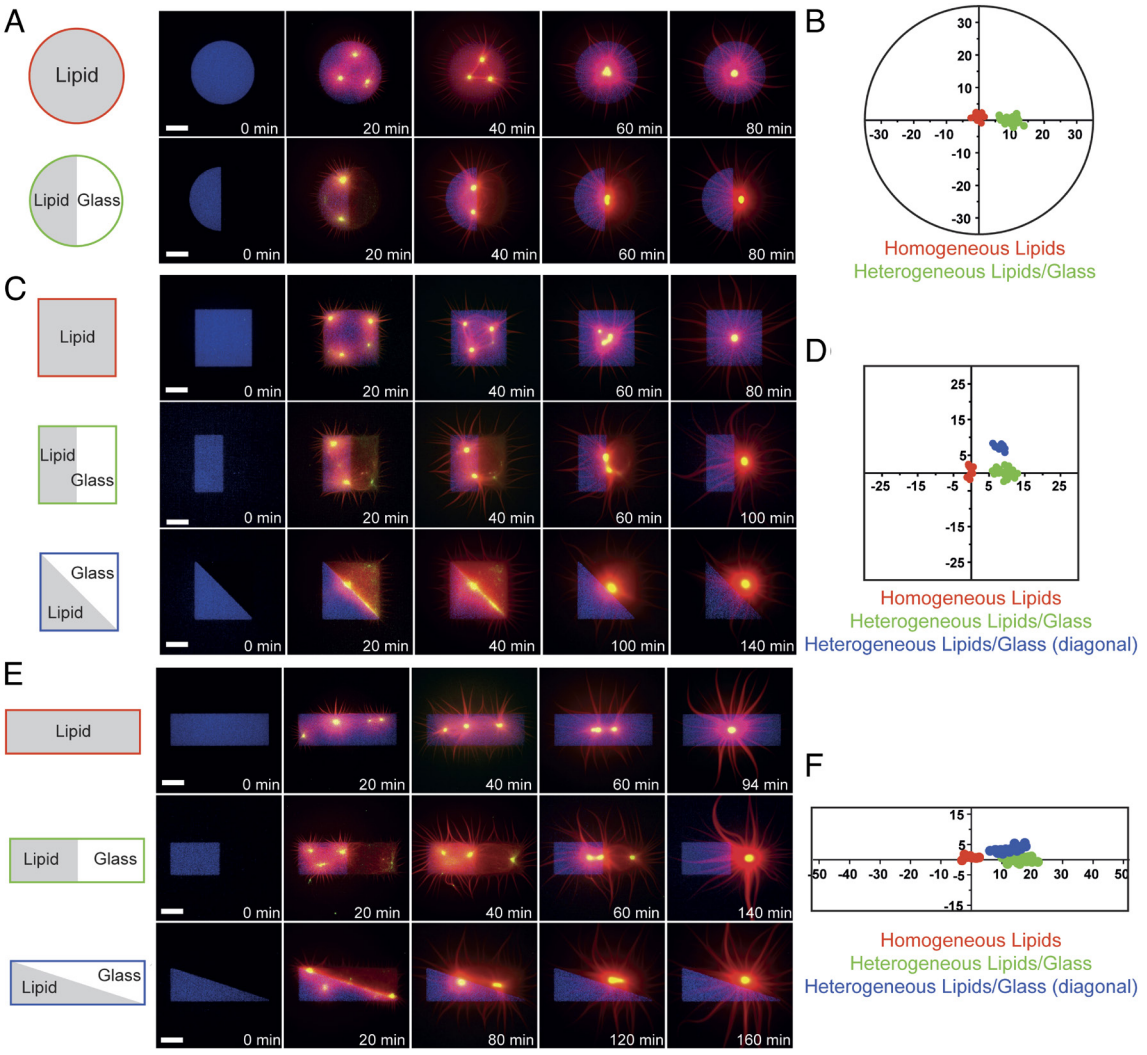

Fig. 4. Friction pattern directs network contraction. Time-lapse imaging of actin network contraction on full lipid or heterogeneous disks (*A*), full lipid or heterogeneous squares (*C*), and full lipid or heterogeneous rectangles (*E*). Biochemical conditions: Actin 1 μM, Human Profilin 3 μM, Arp2/3 complex 25 nM, and Myosin VI 10 nM. Pattern dimensions: disks 64 μm diameter; squares 60 μm length; rectangles 104 μm × 34 μm. The pattern is represented in blue, actin in red, and myosin in green. (Scale bar: 20 μm.) (*B*, *D*, and *F*) Plot of the myosin dots coordinates at the end of contraction for the different shapes. All coordinates were measured and compared to the centroid (x = 0, y = 0) of the whole pattern. Red dots correspond to the coordinates of the full pattern made of lipid, green dots correspond to the coordinates of the symmetrical heterogeneous pattern and the blue dots correspond to the coordinates of the asymmetrical heterogeneous patterns. Disk full lipids: N = 3, n = 11 patterns. Heterogeneous disk: N = 4, n = 26 patterns. Square full lipids: N = 2, n = 9 patterns. Heterogeneous square: N = 4, n = 29 patterns. Asymmetrical heterogeneous square: N = 2, n = 11 patterns. Rectangle full lipids: N = 2, n = 8 patterns. Heterogeneous rectangle: N = 4, n = 24 patterns. Asymmetrical heterogeneous rectangle: N = 3, n = 21 patterns.

impact of the asymmetry of myosin distribution. They also showed that myosin foci first moved along angle bisecting lines and then reorient toward the rectangle center. These observations were also consistent with the model (Fig. 5 *C* and *E* and *SI Appendix*, Fig. S9 *E* and *F*) and further demonstrated that the contraction process integrate local and global network geometry, as previously shown (10), regardless of the initial pattern of myosins.

Importantly, during the contraction of actin networks assembled on heterogeneous square patterns of glass and lipids, we also found that myosin foci could be observed above both types of substrates (Fig. 6*C* and Movies S11 and S12). This confirmed that network density and architectures were similar on glass and on lipids and that the initial localization of myosin foci was not determined by the strength of the underlying friction. The trajectories were initially not all directed toward network final convergence point, likely due to the asynchrony of the contraction described earlier (Fig. 2) but then all move toward the off-centered destination regardless of their position above glass or lipids, further confirming that the network integrated the entire geometry and the entire heterogeneity of the underlying friction pattern (Fig. 6*C*). Foci trajectories during the contraction of actin networks assembled on heterogeneous rectangular patterns of glass and lipids confirmed these two conclusions on the dominant roles of network geometry and friction pattern over the initial distribution of myosins (Fig. 6*D*).

Discussion

Actin network architecture, myosin distribution, and network anchorages are intimately related. They coassemble and influence each other in complex feedback loops. Indeed, adhesion primes filament assembly (78, 79), dense filament areas recruit more myosins (80, 81) and contractile forces promote the enlargement of adhesions (82, 83). It is therefore difficult to attribute the deformation process of the contracting network to one or the other parameter. Most of previous works were focused on the steering

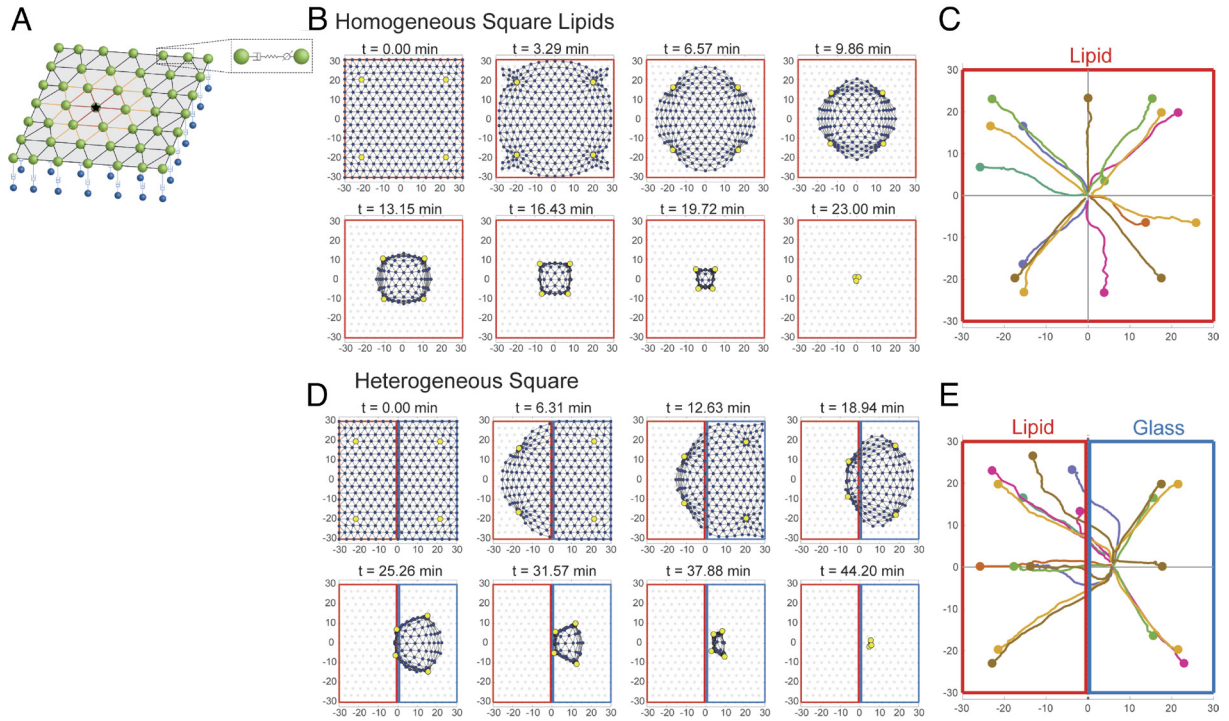

Fig. 5. The computational model recapitulates the contraction kinetics and predicts the trajectories of myosin spots during the network contraction. (*A*) Scheme of the computational model describing the network as a viscoelastic network of nodes and links. Each node is connected by a dashpot with the substrate. The dashpot is responsible for the friction (higher on glass, lower on lipid). Neighboring nodes are connected by dashpot/spring in series responsible for viscous and elastic deformations inside the network. In addition, links connecting pairs of nodes, one of which is occupied by a myosin dot (shown by a star), are contractile. (*B*) Sequence of deformations predicted by the model for an actin network polymerized on a homogeneous square lipid micropattern and contracted by myosin dots (yellow nodes). (*C*) Prediction of myosin trajectories for an actin network contracting on a homogeneous square lipid micropattern. (*D*) Sequence of deformations predicted by the model for an actin network polymerized on a heterogeneous square micropattern and contracted by myosin dots (yellow nodes). (*E*) Prediction of myosin trajectories for an actin network contracting on a heterogeneous square micropattern.

role of motors distribution since it powers the contraction process (84, 85). In vitro experiments revealed the role of network architecture in modulating the rate of network deformation by its impact on the connectivity of the contractile network (13, 72, 75).

Our study uses micropatterns on two different substrates (glass and lipids) which exhibit different frictions to precisely control the initial geometry and density of the actin network. This enabled us to study the symmetry of contraction in these conditions with respect to the initial actin network geometry. We have shown that contraction ends at the centroid of the pattern with uniform friction. We have also shown that friction is a key player in controlling contraction velocity (Figs. 2 and 3) where previous work studied the role of network cross-linking to the surface on its contraction (67, 86, 87).

By developing a method to create heterogeneous micropatterns with different boundary between regions of different friction, we have demonstrated that the pattern of friction drives the contraction asymmetry and more importantly that the friction pattern dominates the contribution of asymmetric distribution of myosins on the patterns (Fig. 6).

Here, we clearly establish the key role of friction pattern in the guidance of network deformation during contraction. This implies for cells and tissues that homogeneous contractile networks, made of even distribution of actin filament and myosins, can contract asymmetrically if their anchorages are not evenly distributed, or if the interaction between the network and its underlying substrate is not identical all over the network.

Our numerical simulations of a viscoelastic contractile network and our experimental data also show the less intuitive result that the friction pattern can guide network contraction in a quite robust manner that dominates the contribution of a heterogeneous distribution of myosins. In physiological conditions, this implies that morphogenetic processes can result from the local recruitment and activation of myosins by signaling but that the role of nonspecific adhesion is also key in the establishment of the final orientation of the deformation process. Thus, both orientations of the powering force and the resistive forces are essentials, as well known by sailors which efficiently combine the use of wind orientation in the sails to propel the boat and the rudder blade orientation to establish its final direction.

Materials and Methods

Protein Expression, Purification, and Labeling. Actin was purified from rabbit skeletal-muscle acetone powder (88). Actin was labeled on lysines with Alexa 568 (89). All experiments were carried out with 5% labeled actin. The Arp2/3 complex was purified from the calf thymus according to ref. 90. Human profilin was expressed in BL21 DE3 pLys *Escherichia coli* cells and purified according to ref. 91. Double-headed porcine myosin VI with bound calmodulin was purified from Sf9 cells by FLAG affinity chromatography (92, 93). Human WASp-WA (Snap-Streptavidin-WA-His) (pET plasmid) was expressed in Rosettas 2 (DE3) pLysS (Merck, 71403) and purified according to ref. 94.

Lipid Micropatterning. Deep UV exposure through a chrome-photomask for 45 s creates micropatterns on Silane-PEG coverslip (*SI Appendix*). The coverslip is then mounted in a 70-μm height flow chamber (with a Silane-PEG slide on top, double-sided tape, Lima ref 1820080). Thirty microliters of SUV lipid solution (*SI Appendix*) is then immediately perfused in the flow chamber. After 10 min of incubation at room temperature, the flow chamber is rinsed with 1 mL of SUV buffer. The diffusivity of the lipid bilayer was checked before each

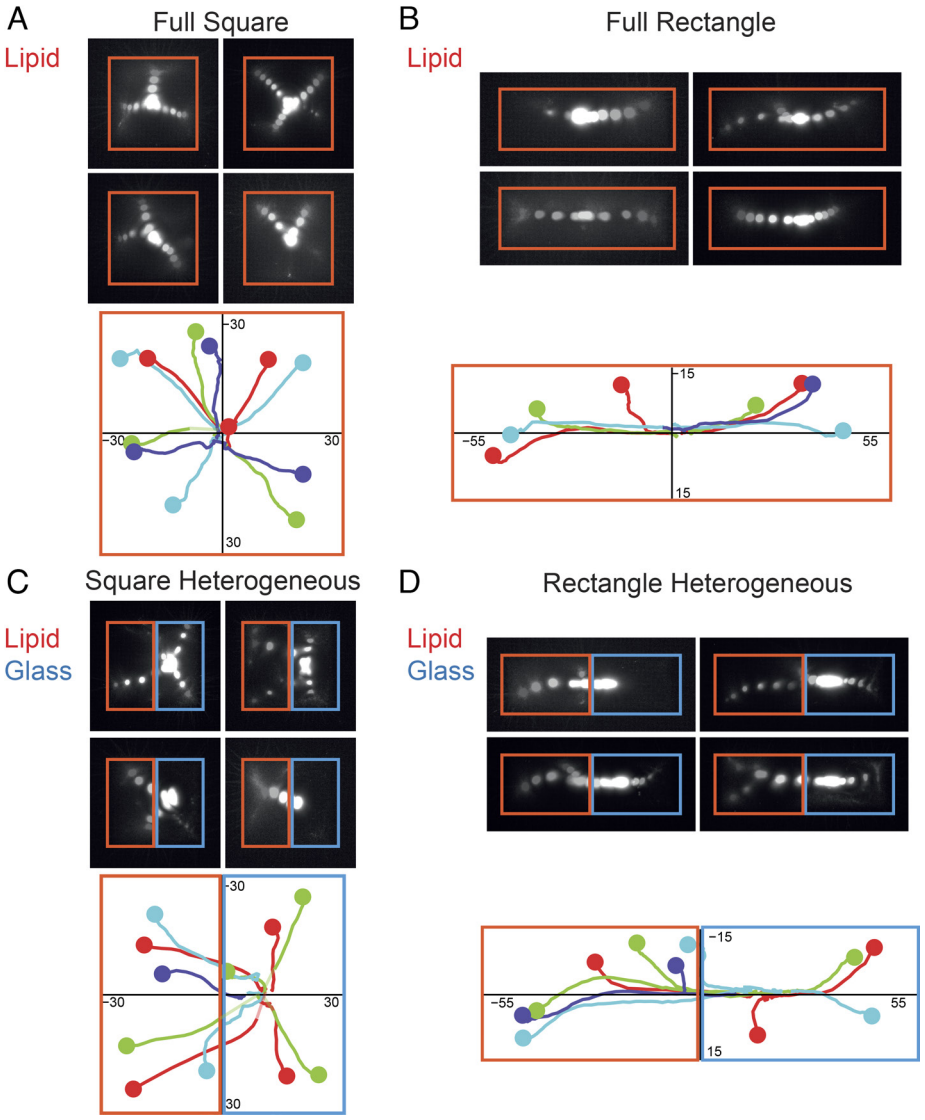

Fig. 6. Friction pattern robustly drives network contraction despite uneven distribution of myosin. *Top*: Four examples of temporal projections of myosin detection on a full-square micropattern (*A*), a full-rectangle micropattern (*B*), a heterogeneous square micropattern (*C*), and a heterogeneous rectangle micropattern (*D*). *Bottom*: Detection of myosin spots as a function of time (see *Materials and Methods* for details). Each example of the above images is represented with a single color. The initial time of the trajectory is represented with a bigger dot.

experiment with Fluorescence Recovery After Photobleaching (FRAP) analysis of the lipid bilayer.

Patterning for Heterogeneity Experiments. Full, symmetrical and asymmetrical patterns were generated on a Nikon eclipse inverted microscope equipped with the Primo Digital Micromirror Device (DMD) (Alveole) (95).

Actin Polymerization and Contraction. Actin polymerization and contraction were induced by injection in the flow chamber of a reaction mixture containing 1 μM actin monomers (12% labeled with Alexa 568), 3 μM profilin, 25 nM Arp2/3 complex, and 14 nM of HMM-myosin VI (GFP labeled). This protein mixture was diluted in freshly prepared buffer containing 10 mM Hepes (pH 7.5), 3 mM ATP, 27 mM DTT, 1 mM EGTA, 50 mM KCl, 5 mM $MgCl_2$, 3 mg/mL glucose, 20 μg/mL catalase, 100 μg/mL glucose oxidase, and 0.25% w/v methylcellulose. The sample was then closed with VALAP to avoid evaporation.

Imaging. Time courses of actin assembly and contraction on homogeneous patterns were acquired on a TIRF microscope (Roper Scientific) equipped with an iLasPulsed system and an Evolve camera (EMCCD 512 × 512, pixel = 16 μm) using a 60× 1.49 objective lens. Microscope and devices were driven by MetaMorph software (Molecular Devices). For heterogeneous patterns, image acquisition was done on a Nikon Eclipse Ti2 inverted microscope equipped with an S Plan fluor ELWD 40×/0,60 objective and a Hamamatsu ORCA Flash 4.0 LT camera. The microscope and equipment were driven by MicroManager software.

Image Analysis. Image analysis was performed using Fiji (96), RStudio, and GraphPad Prism.

Statistical Analysis. We used Mann–Whitney tests (nonparametric test) performed in GraphPad Prism software.

Computational Modeling. We model the actomyosin network as a contractile viscoelastic medium represented by a lattice of actin and myosin nodes connected to each other by spring-like links and to the substrate by adhesive dashpots. The network's deformations are simulated numerically by solving force balance equations. Details of the model and numerical solutions are in *SI Appendix*.

Data, Materials, and Software Availability. All study data are included in the article and/or supporting information.

ACKNOWLEDGMENTS. We thank C. Copos for help with modeling. This work was supported by the European Research Council [Consolidator Grant 771599 (ICEBERG) awarded to M.T. and Advanced Grant 741773 (Adaptive Actin

Architectures) awarded to L.B.]. This work was also supported by the MuLife imaging facility, which is funded by Grenoble Alliance for Integrated Structural, a program from the Chemistry Biology Health Graduate School of University Grenoble Alpes (ANR-17-EURE-0003). M.S. and A.M. were supported by NSF grant DMS 1953430 and 2052515 awarded to A.M. E.M.D.L.C. and W.C. were supported by the NIH through award R35-GM136656 awarded to E.M.D.L.C.

Author affiliations: [a]Université Grenoble-Alpes, CEA, CNRS, UMR5168, Interdisciplinary Research Institute of Grenoble, CytoMorpho Lab, Grenoble 38054, France; [b]Courant Institute of Mathematical Sciences, New York University, New York, NY 10012; [c]Department of Molecular Biophysics and Biochemistry, Yale University, New Haven, CT 06520-8114; [d]University of Paris, INSERM, Commissariat à l'énergie atomique et aux énergies alternatives, UMRS1160, Institut de Recherche Saint Louis, CytoMorpho Lab, Hôpital Saint Louis, Paris 75010, France; and [e]Department of Biochemistry, University of Geneva, CH-1211 Geneva, Switzerland

1. M. Kollmar, S. Mühlhausen, Myosin repertoire expansion coincides with eukaryotic diversification in the Mesoproterozoic era. *BMC Evol. Biol.* **17**, 211 (2017).
2. M. A. Hartman, J. A. Spudich, The myosin superfamily at a glance. *J. Cell Sci.* **125**, 1627–1632 (2012).
3. B. Wickstead, K. Gull, The evolution of the cytoskeleton. *J. Cell Biol.* **194**, 513–525 (2011).
4. J. R. Sellers, Myosins: A diverse superfamily. *Biochim. Biophys. Acta–Mol. Cell Res.* **1499**, 3–22 (2000).
5. J. Robert-Paganin, O. Pylypenko, C. Kikuti, H. L. Sweeney, A. Houdusse, Force generation by myosin motors: A structural perspective. *Chem. Rev.* **120**, 5–35 (2020).
6. L. Blanchoin, R. Boujemaa-Paterski, C. Sykes, J. Plastino, Actin dynamics, architecture, and mechanics in cell motility. *Physiol. Rev.* **94**, 235–263 (2014).
7. M. Murrell, P. W. Oakes, M. Lenz, M. L. Gardel, Forcing cells into shape: The mechanics of actomyosin contractility. *Nat. Rev. Mol. Cell Biol.* **16**, 486–498 (2015).
8. C.-P.P. Heisenberg, Y. Bellaïche, Forces in tissue morphogenesis and patterning. *Cell* **153**, 948–962 (2013).
9. D. N. Clarke, A. C. Martin, Actin-based force generation and cell adhesion in tissue morphogenesis. *Curr. Biol.* **31**, R667–R680 (2021).
10. M. Schuppler, F. C. Keber, M. Kröger, A. R. Bausch, Boundaries steer the contraction of active gels. *Nat. Commun.* **7**, 13120 (2016).
11. L. Kurzawa *et al.*, Dissipation of contractile forces: The missing piece in cell mechanics. *Mol. Biol. Cell* **28**, 1825–1832 (2017).
12. L. B. Case, C. M. Waterman, Integration of actin dynamics and cell adhesion by a three-dimensional, mechanosensitive molecular clutch. *Nat. Cell Biol.* **17**, 955–963 (2015).
13. A.-C. Reymann *et al.*, Actin network architecture can determine myosin motor activity. *Science* **336**, 1310–1314 (2012).
14. K. M. Yamada, M. Sixt, Mechanisms of 3D cell migration. *Nat. Rev. Mol. Cell Biol.* **20**, 738–752 (2019).
15. M. Schaks, G. Giannone, K. Rottner, Actin dynamics in cell migration. *Essays Biochem.* **63**, 483–495 (2019).
16. M. Bornens, M. Paintrand, C. Celati, The cortical microfilament system of lymphoblasts displays a periodic oscillatory activity in the absence of microtubules: Implications for cell polarity. *J. Cell Biol.* **109**, 1071–1083 (1989).
17. E. Paluch, M. Piel, J. Prost, M. Bornens, C. Sykes, Cortical actomyosin breakage triggers shape oscillations in cells and cell fragments. *Biophys. J.* **89**, 724–733 (2005).
18. W. Shih, S. Yamada, Myosin IIA dependent retrograde flow drives 3D cell migration. *Biophys. J.* **98**, L29–L31 (2010).
19. P. Maiuri *et al.*, Actin flows mediate a universal coupling between cell speed and cell persistence. *Cell* **161**, 374–386 (2015).
20. P. R. O'Neill *et al.*, Membrane flow drives an adhesion-independent amoeboid cell migration mode. *Dev. Cell* **46**, 9–22.e4 (2018).
21. S. de Beco *et al.*, Optogenetic dissection of Rac1 and Cdc42 gradient shaping. *Nat. Commun.* **9**, 1–13 (2018).
22. A. Mehidi *et al.*, Transient activations of Rac1 at the lamellipodium tip trigger membrane protrusion. *Curr. Biol.* **29**, 2852–2866.e5 (2019).
23. W. M. Bement *et al.*, Activator–inhibitor coupling between Rho signalling and actin assembly makes the cell cortex an excitable medium. *Nat. Cell Biol.* **17**, 1471–1483 (2015).
24. M. Graessl *et al.*, An excitable Rho GTPase signaling network generates dynamic subcellular contraction patterns. *J. Cell Biol.* **216**, 4271–4285 (2017).
25. E. L. Barnhart, K.-C. Lee, K. Keren, A. Mogilner, J. A. Theriot, An adhesion-dependent switch between mechanisms that determine motile cell shape. *PLoS Biol.* **9**, e1001059 (2011).
26. E. L. Barnhart, K.-C. Lee, G. M. Allen, J. A. Theriot, A. Mogilner, Balance between cell–substrate adhesion and myosin contraction determines the frequency of motility initiation in fish keratocytes. *Proc. Natl. Acad. Sci. U.S.A.* **112**, 5045–5050 (2015).
27. H. Blaser *et al.*, Migration of zebrafish primordial germ cells: A role for myosin contraction and cytoplasmic flow. *Dev. Cell* **11**, 613–627 (2006).
28. D. T. Burnette *et al.*, A role for actin arcs in the leading-edge advance of migrating cells. *Nat. Cell Biol.* **13**, 371–382 (2011).
29. J. R. Beach *et al.*, Actin dynamics and competition for myosin monomer govern the sequential amplification of myosin filaments. *Nat. Cell Biol.* **19**, 85–93 (2017).
30. L. Yolland *et al.*, Persistent and polarized global actin flow is essential for directionality during cell migration. *Nat. Cell Biol.* **21**, 1370–1381 (2019).
31. Q. Yang, X.-F. Zhang, T. D. Pollard, P. Forscher, Arp2/3 complex-dependent actin networks constrain myosin II function in driving retrograde actin flow. *J. Cell Biol.* **197**, 939–956 (2012), 10.1083/jcb.201111052.
32. V. Ruprecht *et al.*, Cortical contractility triggers a stochastic switch to fast amoeboid cell motility. *Cell* **160**, 673–685 (2015).
33. L. Barbier *et al.*, Myosin II activity is selectively needed for migration in highly confined microenvironments in mature dendritic cells. *Front. Immunol.* **10**, 1–9 (2019).
34. M. Chabaud *et al.*, Cell migration and antigen capture are antagonistic processes coupled by myosin II in dendritic cells. *Nat. Commun.* **6**, 7526 (2015).
35. L. Valon, A. Marín-Llauradó, T. Wyatt, G. Charras, X. Trepat, Optogenetic control of cellular forces and mechanotransduction. *Nat. Commun.* **8**, 14396 (2017).
36. P. W. Oakes *et al.*, Optogenetic control of RhoA reveals zyxin-mediated elasticity of stress fibres. *Nat. Commun.* **8**, 15817 (2017).
37. K. Hennig *et al.*, Stick-slip dynamics of cell adhesion triggers spontaneous symmetry breaking and directional migration of mesenchymal cells on one-dimensional lines. *Sci. Adv.* **6**, 1–13 (2020).
38. M. Rauzi, P. Verant, T. Lecuit, P.-F. Lenne, Nature and anisotropy of cortical forces orienting Drosophila tissue morphogenesis. *Nat. Cell Biol.* **10**, 1401–1410 (2008).
39. M. Rauzi, P.-F. Lenne, T. Lecuit, Planar polarized actomyosin contractile flows control epithelial junction remodelling. *Nature* **468**, 1110–1114 (2010).
40. N. L. Nerurkar, C. H. Lee, L. Mahadevan, C. J. Tabin, Molecular control of macroscopic forces drives formation of the vertebrate hindgut. *Nature* **565**, 480–484 (2019).
41. N. C. Heer *et al.*, Actomyosin-based tissue folding requires a multicellular myosin gradient. *J. Cell Sci.* **130**, 1876–1886 (2017).
42. T. Vignaud *et al.*, Stress fibres are embedded in a contractile cortical network. *Nat. Mater.* **20**, 410–420 (2021).
43. J. I. Lehtimäki, E. K. Rajakylä, S. Tojkander, P. Lappalainen, Generation of stress fibers through myosin-driven reorganization of the actin cortex. *Elife* **10**, 1–43 (2021).
44. J. Colombelli *et al.*, Mechanosensing in actin stress fibers revealed by a close correlation between force and protein localization. *J. Cell Sci.* **122**, 1665–1679 (2009).
45. M. Théry, A. Pépin, E. Dressaire, Y. Chen, M. Bornens, Cell distribution of stress fibres in response to the geometry of the adhesive environment. *Cell Motil. Cytoskeleton* **63**, 341–355 (2006).
46. K. Mandal, A. Asnacios, B. Goud, J.-B. Manneville, Mapping intracellular mechanics on micropatterned substrates. *Proc. Natl. Acad. Sci. U.S.A.* **113**, E7159–E7168 (2016).
47. T. J. Autenrieth *et al.*, Actomyosin contractility and RhoGTPases affect cell-polarity and directional migration during haptotaxis. *Integr. Biol. (Camb).* **8**, 1067–1078 (2016).
48. F. Senger *et al.*, Spatial integration of mechanical forces by α-actinin establishes actin network symmetry. *J. Cell Sci.* **132**, jcs236604 (2019).
49. A. B. Verkhovsky, T. M. Svitkina, G. G. Borisy, Self-polarization and directional motility of cytoplasm. *Curr. Biol.* **9**, 11–20 (1999).
50. Y. Aratyn-Schaus, M. L. Gardel, Transient frictional slip between integrin and the ECM in focal adhesions under myosin II tension. *Curr. Biol.* **20**, 1145–1153 (2010).
51. I. Linsmeier *et al.*, Disordered actomyosin networks are sufficient to produce cooperative and telescopic contractility. *Nat. Commun.* **7**, 12615 (2016).
52. M. F. Fournier, R. Sauser, D. Ambrosi, J.-J. Meister, A. B. Verkhovsky, Force transmission in migrating cells. *J. Cell Biol.* **188**, 287–297 (2010).
53. P. Nordenfelt, H. L. Elliott, T. A. Springer, Coordinated integrin activation by actin-dependent force during T-cell migration. *Nat. Commun.* **7**, 1–15 (2016).
54. M. P. Murrell, M. L. Gardel, Actomyosin sliding is attenuated in contractile biomimetic cortices. *Mol. Biol. Cell* **25**, 1845–1853 (2014).
55. E. Hannezo, B. Dong, P. Recho, J.-F. Joanny, S. Hayashi, Cortical instability drives periodic supracellular actin pattern formation in epithelial tubes. *Proc. Natl. Acad. Sci. U.S.A.* **112**, 201504762 (2015).
56. M. Bergert *et al.*, Force transmission during adhesion-independent migration. *Nat. Cell Biol.* **17**, 524–529 (2015).
57. A. Reversat *et al.*, Cellular locomotion using environmental topography. *Nature* **582**, 582–585 (2020).
58. R. Sakamoto, Z. Izri, Y. Shimamoto, M. Miyazaki, Y. T. Maeda, Geometric trade-off between contractile force and viscous drag determines the actomyosin-based motility of a cell-sized droplet. *Proc. Natl. Acad. Sci. U.S.A.* **119**, e2121147119 (2022).
59. C. M. Lo, H. B. Wang, M. Dembo, Y.-L. Wang, Cell movement is guided by the rigidity of the substrate. *Biophys. J.* **79**, 144–152 (2000).
60. M. L. Gardel *et al.*, Traction stress in focal adhesions correlates biphasically with actin retrograde flow speed. *J. Cell Biol.* **183**, 999–1005 (2008).
61. R. Sunyer *et al.*, Collective cell durotaxis emerges from long-range intercellular force transmission. *Science* **353**, 1157–1161 (2016).
62. S. Chanet *et al.*, Actomyosin meshwork mechanosensing enables tissue shape to orient cell force. *Nat. Commun.* **8**, 15014 (2017).
63. M. Smutny *et al.*, Friction forces position the neural anlage. *Nat. Cell Biol.* **19**, 306–317 (2017).
64. L. G. Pimpale, T. C. Middelkoop, A. Mietke, S. W. Grill, Cell lineage-dependent chiral actomyosin flows drive cellular rearrangements in early Caenorhabditis elegans development. *Elife* **9**, 842922 (2020).
65. D. Pinheiro *et al.*, Transmission of cytokinesis forces via E-cadherin dilution and actomyosin flows. *Nature* **545**, 103–107 (2017).
66. A.C. Reymann *et al.*, Nucleation geometry governs ordered actin networks structures. *Nat. Mater.* **9**, 827–832 (2010).
67. M. P. Murrell, M. L. Gardel, F-actin buckling coordinates contractility and severing in a biomimetic actomyosin cortex. *Proc. Natl. Acad. Sci. U.S.A.* **109**, 20820–20825 (2012).
68. E. L. Suzuki *et al.*, Geometrical constraints greatly hinder formin mDia1 activity. *Nano Lett.* **20**, 22–32 (2020).
69. A. Azioune, M. Storch, M. Bornens, M. Théry, M. Piel, Simple and rapid process for single cell micropatterning. *Lab Chip* **9**, 1640–1642 (2009).
70. L. C. Kam, S. G. Boxer, Cell adhesion to protein-micropatterned-supported lipid bilayer membranes. *J. Biomed. Mater. Res.* **55**, 487–495 (2001).
71. Sonal *et al.*, Myosin-II activity generates a dynamic steady state with continuous actin turnover in a minimal actin cortex. *J. Cell Sci.* **132**, jcs219899 (2019).
72. C. G. Muresan *et al.*, F-actin architecture determines constraints on myosin thick filament motion. *Nat. Commun.* **13**, 7008 (2022).
73. R. Grover *et al.*, Transport efficiency of membrane-anchored kinesin-1 motors depends on motor density and diffusivity. *Proc. Natl. Acad. Sci. U.S.A.* **113**, E7185–E7193 (2016).
74. A. Sciortino, A. R. Bausch, Pattern formation and polarity sorting of driven actin filaments on lipid membranes. *Proc. Natl. Acad. Sci. U.S.A.* **118**, e2017047118 (2021).

75. H. Ennomani *et al.*, Architecture and connectivity govern actin network contractility. *Curr. Biol.* **26**, 616–626 (2016).
76. B. A. Smith *et al.*, Three-color single molecule imaging shows WASP detachment from Arp2/3 complex triggers actin filament branch formation. *Elife* **2**, e01008 (2013).
77. M. Soares e silva, B. Stuhrmann, T. Betz, G. H. Koenderink, Time-resolved microrheology of actively remodeling actomyosin networks. *New J. Phys.* **16**, 075010 (2014).
78. E. M. Kovacs, M. Goodwin, R. G. Ali, A. D. Paterson, A. S. Yap, Cadherin-directed actin assembly: E-cadherin physically associates with the Arp2/3 complex to direct actin assembly in nascent adhesive contacts. *Curr. Biol.* **12**, 379–382 (2002).
79. B. Serrels *et al.*, Focal adhesion kinase controls actin assembly via a FERM-mediated interaction with the Arp2/3 complex. *Nat. Cell Biol.* **9**, 1046–1056 (2007).
80. I. M. Herman, N. J. Crisona, T. D. Pollard, Relation between cell activity and the distribution of cytoplasmic actin and myosin. *J. Cell Biol.* **90**, 84–91 (1981).
81. M. Raab *et al.*, Crawling from soft to stiff matrix polarizes the cytoskeleton and phosphoregulates myosin-II heavy chain. *J. Cell Biol.* **199**, 669–683 (2012).
82. D. Riveline *et al.*, Focal contacts as mechanosensors: Externally applied local mechanical force induces growth of focal contacts by an mDia1-dependent and ROCK-independent mechanism. *J. Cell Biol.* **153**, 1175–1186 (2001).
83. G. Giannone *et al.*, Lamellipodial actin mechanically links myosin activity with adhesion-site formation. *Cell* **128**, 561–575 (2007).
84. S. J. Streichan, M. F. Lefebvre, N. Noll, E. F. Wieschaus, B. I. Shraiman, Global morphogenetic flow is accurately predicted by the spatial distribution of myosin motors. *Elife* **7**, e27454 (2018).
85. C. R. Cowan, A. A. Hyman, Acto-myosin reorganization and PAR polarity in C. elegans. *Development* **134**, 1035–1043 (2007).
86. S. K. Vogel, Z. Petrasek, F. Heinemann, P. Schwille, Myosin motors fragment and compact membrane-bound actin filaments. *Elife* **2**, e00116 (2013).
87. K. Carvalho *et al.*, Cell-sized liposomes reveal how actomyosin cortical tension drives shape change. *Proc. Natl. Acad. Sci. U.S.A.* **110**, 16456–16461 (2013).
88. J. A. Spudich, S. Watt, The regulation of rabbit skeletal muscle contraction. I. Biochemical studies of the interaction of the tropomyosin-troponin complex with actin and the proteolytic fragments of myosin. *J. Biol. Chem.* **246**, 4866–4871 (1971).
89. H. Isambert *et al.*, Flexibility of actin filaments derived from thermal fluctuations. *J. Biol. Chem.* **270**, 11437–11444 (1995).
90. C. Egile *et al.*, Activation of the Cdc42 Effector N-Wasp by the Shigella flexneri Icsa protein promotes actin nucleation by Arp2/3 complex and bacterial actin-based motility. *J. Cell Biol.* **146**, 1319–1332 (1999).
91. S. C. Almo, T. D. Pollard, M. Way, E. E. Lattman, Purification, characterization and crystallization of Acanthamoeba profilin expressed in Escherichia coli. *J. Mol. Biol.* **236**, 950–952 (1994).
92. J. P. Robblee, A. O. Olivares, E. M. De La Cruz, Mechanism of nucleotide binding to actomyosin VI. *J. Biol. Chem.* **279**, 38608–38617 (2004).
93. E. M. De La Cruz, E. M. Ostap, H. L. Sweeney, Kinetic mechanism and regulation of myosin VI. *J. Biol. Chem.* **276**, 32373–32381 (2001).
94. A. Colin *et al.*, Recycling of the actin monomer pool limits the lifetime of network turnover. *EMBO J.* **42**, e112717 (2023).
95. P. O. Strale *et al.*, Multiprotein printing by light-induced molecular adsorption. *Adv. Mater.* **28**, 2024–2029 (2016).
96. J. Schindelin *et al.*, Fiji: An open-source platform for biological-image analysis. *Nat. Methods* **9**, 676–682 (2012).

Friction patterns guide actin network contraction

Alexandra Colin[1]*, Magali Orhant-Prioux[1]*, Christophe Guérin[1]*, Mariya Savinov[2]*, Wenxiang Cao[4], Benoit Vianay[5], Ilaria Scarfone[1], Aurelien Roux[3], Enrique M. De La Cruz[4], Alex Mogilner[2], Manuel Théry[1,5#], Laurent Blanchoin[1,5#]

1- Univ. Grenoble-Alpes, CEA, CNRS, UMR5168, Interdisciplinary Research Institute of Grenoble, CytoMorpho Lab, 17 rue des Martyrs, 38054 Grenoble, France.
2- Courant Institute of Mathematical Sciences, New York University, New York, NY 10012, United States.
3- Department of Biochemistry, University of Geneva, Geneva, Switzerland.
4- Department of Molecular Biophysics and Biochemistry, Yale University, 260 Whitney Avenue, New Haven, CT 06520-8114, United States.
5- Univ. Paris, INSERM, CEA, UMRS1160, Institut de Recherche Saint Louis, CytoMorpho Lab, Hôpital Saint Louis, 10 Avenue Claude Vellefaux, 75010 Paris, France.

* these authors contributed equally to this work
# Correspondence should be sent to: manuel.thery@cea.fr, laurent.blanchoin@cea.fr

Supporting information

This file includes:

Supporting text (description of methods and model, pages 2-16)

Figures S1 to S9 (pages 17-26)

Legends for Movies S1 to S19 (pages 27-29)

Supporting References (page 30)

Supporting Text

Description of methods and model

SUV (small unilamellar vesicules) preparation

L-α-phosphatidylcholine (EggPC) (Avanti, 840051C), DSPE-PEG(2000) Biotin (1,2-distearoyl-sn-glycero-3 phosphoethanolamine-N-[biotinyl(polyethylene glycol)-2000], ammonium salt, Avanti, : 880129C-10mg chloroforme) and ATTO 647N labeled DOPE (ATTO-TEC, AD 647N-161 dehydrated) were used. Lipids were mixed in glass tubes as follows: 98.75% EggPC (10 mg/mL), 0.25% DSPE-PEG(2000) Biotin (10 mg/mL) and 1% DOPE-ATTO390 (1 mg/mL). The mixture was dried with nitrogen gas. The dried lipids were incubated under vacuum overnight. After that, the lipids were hydrated in the SUV buffer (10 mM Tris (pH 7.4), 150 mM NaCl, 2 mM $CaCl_2$). The mixture was sonicated on ice for 10 minutes. The mixture was then centrifuged for 10 min at 20,238 x g to remove large structures. The supernatants were collected and stored at 4°C until use.

Preparation of SilanePEG passivated slides

SilanePEG (30kDa, PSB-2014 or 5 kDa, PLS-2011, Creative PEG works) was prepared at a final concentration of 1 mg/mL in 96% ethanol and 0.1%(v/v) HCl. Slides and coverslips were cleaned with the following protocol: they were sonicated for 30 minutes at 60°C in Hellmanex 2%. They were then rinsed with several volumes of mqH2O. Just before use, they were dried with compressed air. Slides and coverslips were plasma cleaned (Femto; Diener Electronic) for 5 minutes at 80% power and directly immersed in the silanePEG solution for 18 hours. They were dried just before use.

Patterning for heterogeneity experiments

A flow chamber made with silanePEG 30k treated glass and cover glass and spaced with a 70 µm double tape was filled with a photo initiator (PLPP). Patterns were designed in Inkscape and loaded into the µmanager's Leonardo plugin (Alveole). The burning was done at 90 mJ at 100% of a 5.6mW 365 nm wavelength laser. The flow chamber was then washed with 600 µl of water to remove the PLPP and 200 µl of SUV Buffer. 40 µl of SUV solution was then added and incubated for 10 minutes at room temperature for an effective lipid coating. The excess of SUV was washed out by passing 600 µl of SUV Buffer. The flow chamber was then passivated with 50 µl of 1% BSA diluted in 1x HKEM. For the symmetrical and asymmetrical patterns, where a second round of patterning is required, 40 µl of PLPP was injected. After a precise alignment, the burning was done at 70mJ at 80% of the laser. The PLPP was removed with 600µl of SUV buffer and equilibrated with 200µl of 1x HKEM. A mixture of 2 NPFs (5nM Strep-WA, 1µM GST-PWA, 0,1% BSA in 1x HKEM) was injected and the coating was done by

letting incubate for 15 minutes at room temperature. The excess of NPFs was washed out by passing 600 µl of 1x HKEM and 30µl of the reaction mixture see below.

Image analysis

Analysis of contraction Area:

Images were cropped according the size of the pattern and then binarized with Otsu method. Actin network area was determined with the "Analyse particles" function in Fiji. On heterogeneous patterns, we determined and analyzed the actin area of each part of the pattern.

For the estimation of the myosin threshold necessary to start the contraction, the myosin intensity at the first time point of the deformation phase was taken and then correlated with the contraction velocity.

PIV Analysis: PIV analysis was performed with the "iterative PIV plugin" in Fiji. The movie was first cropped around the pattern. We did the analysis on pairs of images taken every 3 frames in the different movies. Then, to analyze the PIV results, we separated the square pattern in four "quadrants" corresponding to the four corners of the square pattern. For each time of the PIV analysis, in each of these quadrants, we summed the vectors to obtain the value of the "PIV displacement" in each quadrant at each time point. Then we plotted this norm of vector sum for each quadrant as a function of time for networks contracting on glass or on lipids.

Myosin spots tracking:

Myosin spots were detected and tracked with TrackMate plugin.

Tracking of single filaments and branches: Movies (3 minutes duration) of single filaments and early events of branches formation were taken with an interval of 3 seconds between the frames. Single filaments and branches were then manually tracked in Fiji using the Manual tracking plugin. Coordinates were retrieved in R software and MSD was computed in R software. A linear fit on the MSD was then done on the first part of the curve (30 seconds) and diffusion coefficient was obtained by dividing the slope value by 4.

Estimation of diffusion coefficient of lipids and WA protein on lipids: FRAP data were analyzed with a custom-written macro in Fiji. Briefly, after correction for bleaching and background, an exponential fit of the fluorescence in the FRAP zone is performed in order to estimate the half-time of recovery ($\tau_{1/2}$). Then, diffusion coefficient is computed from the following equation: $D = \frac{r^2}{4\tau_{1/2}}\gamma_D$ with r: radius of the bleached area and γ_D the diffusion constant ($\gamma_D = 0.88$).

Mechanical model of contractile adhesive actomyosin network

Qualitative model description

We model the actomyosin network *as a two-dimensional active viscoelastic material*. It is well established that actin networks exhibit viscoelastic properties, with elastic behaviors predominantly seen at short timescales (seconds to tens of seconds) and viscous effects at long timescales (tens of seconds and longer) due to actin filament turnover and stochastic binding dynamics of crosslinks between filaments (1, 2). So, we model the system as *elastic with relaxation* (such that elastic stresses dissipate with time) and with active myosin contraction. The relaxation leads to viscous behavior on longer timescales. We also consider a nonlinear elasticity where the response to compression is disproportionately weaker than the response to stretch (see below). The deforming actomyosin network in the model experiences an *effective viscous drag (friction) relative to the substrate*.

The actomyosin mesh is coarse-grained as a triangular network of nodes connected by approximately equal length links. The links consist of a relaxing elastic spring (similar to the Maxwell element – elastic spring and viscous dashpot) ~~Maxwell element (elastic spring and viscous dashpot)~~ and a contractile element in series (Figure 5A). The contractile elements yield a contractile tension determined by the myosin distribution. Each node is connected to the substrate by a viscous dashpot representing the friction between the network and substrate.

Elastic Forces

Consider a node i, linked to a neighboring node j. The link is modeled as an elastic spring that has rest length ℓ_{ij}^0 and current length $\ell_{ij} = |\boldsymbol{x_i} - \boldsymbol{x_j}|$. The force magnitude exerted on node i by the spring connecting node i to node j, in series with a contractile element, is

$$F_{ij}^e = \gamma_{ij} + k_{ij}\left(\frac{\ell_{ij}}{\ell_{ij}^0} - 1\right) \qquad (1)$$

This force points from node i to node j, along the unit vector $\boldsymbol{\tau_{ij}}$ connecting the nodes. The first term γ_{ij} is the active contractile ($\gamma_{ij} > 0$) force generated by myosin. Given a normalized myosin distribution at a given time $m(\boldsymbol{x})/m_0$, nodes are assigned 'myosin weights' $\gamma_i = \gamma_0 m(\boldsymbol{x})/m_0$ and the links between nodes are assigned the force equal to average of these weights: $\gamma_{ij} = (\gamma_i + \gamma_j)/2$. This is a simple way to capture the dependence of the contractile force from a myosin distribution on nodes.

The second term in Eq. (1) is a spring force, which depends only on the deviation of the current length ℓ_{ij} from the rest length ℓ_{ij}^0. Following (3), the spring constant k_{ij} has units of force. In the case of a linear elastic isotropic material, this link stiffness can be related to the material elastic modulus λ_E (recall that in 2D, elastic moduli are reported with units $\sim pN/nm$) by equating the discrete strain energy with the continuous strain energy density in the limit of an infinitesimal deformation (3). For a regular mesh of equilateral triangles, such a computation yields a link spring constant

$$K_{ij} = \frac{8\lambda_E}{3\ell_{ij}^0}\left(\frac{dA_i + dA_j}{2}\right) \qquad (2)$$

Here, dA_i is the area weight of node i (the sum of one third of the area of each triangle with vertex $\boldsymbol{x_i}$). In this framework, the associated force density at node i due to the spring between nodes i and j would be $\widetilde{F_{ij}^e} = F_{ij}^e/dA_i$.

We go beyond just Eq. (2) to model the network as nonlinearly elastic. Specifically, we assume that the spring constant is a function of the ratio ℓ_{ij}/ℓ_{ij}^0, as follows:

$$k_{ij} = \begin{cases} K_{ij}, \ \frac{\ell_{ij}}{\ell_{ij}^0} - 1 \geq 0 \\ r_k K_{ij}, \ \frac{\ell_{ij}}{\ell_{ij}^0} - 1 < 0 \end{cases} \quad (3)$$

Thus, *the spring responds to stretching ($\ell_{ij}/\ell_{ij}^0 > 1$) and compression ($\ell_{ij}/\ell_{ij}^0 < 1$) differently*. Here K_{ij} is initialized as in Eq. (2). Parameter r_k is strictly less than 1, so the network can be easily contracted but resists stretching. This nonlinear feature is inspired by modeling the actin mesh as a 'cable' network (4): individual actin filaments and bundles of filaments are not stretchable but can easily bend or buckle.

Force Balance

The internal network forces (active myosin stress and passive elastic forces) are balanced by the friction with the substrate, which is characterized by a drag coefficient ζ which may depend on position. The governing force balance equation for node i is then:

$$\Sigma_{\text{neighbors } j} \left(\gamma_{ij} + k_{ij} \left(\frac{\ell_{ij}}{\ell_{ij}^0} - 1 \right) \right) \boldsymbol{\tau_{ij}} = \zeta \, dA_i \frac{d\boldsymbol{x_i}}{dt} \quad (4)$$

Note that the drag on a node i depends also on its area weight dA_i – essentially, we assume the effective drag on a node to be proportional to its actin density. Since the bulk network is initialized to be uniform, the initial area weight dA_i is a proxy for actin density. So thus, a node with a higher actin density or approximating a larger portion of the network (both yielding more area weight dA_i) should experience more effective drag.

Network relaxation

Thus far, Eq. (1) – (4) describe a nonlinear elastic network. We model the relaxation of the elastic stresses, represented by the dashpot element of links in main text Fig. 5a, by the relaxation of the rest length of elastic springs ℓ_{ij}^0 to their current length with rate r:

$$\frac{d\ell_{ij}^0}{dt} = r(\ell_{ij} - \ell_{ij}^0) \quad (5)$$

For example, if the current length is fixed to be larger than the rest length $\ell_{ij} > \ell_{ij}^0$, then over time ℓ_{ij}^0 will grow until it reaches ℓ_{ij}. Similarly, if the current length is shorter than the rest length $\ell_{ij} < \ell_{ij}^0$, then the rest length will shrink until it reaches ℓ_{ij}.

Since the link spring constants k_{ij} are initialized using Eq. (2) and (3), there is an inherent dependence of the spring constant on the rest lengths local to a node. Presuming that throughout time links are approximately equal locally, this dependence is approximated as $k_{ij} \propto \ell_{ij}^0$. So, as the rest length ℓ_{ij}^0 changes with time, the value k_{ij}/ℓ_{ij}^0 is kept constant for each link. This ensures that the global elastic properties of the network are approximately constant over time, despite relaxation effects.

Myosin contractile forces

Most of the myosin concentration is highly localized into several aggregates (spots). One or several myosin foci appear at locations that we glean from the experiments. Each myosin foci generates radially symmetric stress that rapidly decreases with distance from the center of the foci (in other words, the stress is relatively local). We consider the following simple description for the myosin-generated stress - a myosin spot which initially forms centered at node i_M. This spot center is advected with the network, meaning it is always attached to node i_M throughout the deformation process. At any given time, links in a region of characteristic radius approximately equal to $2\sigma_M$ experience a nonzero tension γ_{ij}. As previously mentioned, each node j is assigned a 'myosin weight' γ_j. For a single myosin spot, this weight γ_j is:

$$\gamma_0 \exp\left(-\left(\frac{x_j - x_{i_M}}{\sigma_M}\right)^2 - \left(\frac{y_j - y_{i_M}}{\sigma_M}\right)^2\right) \qquad (6)$$

The links between nodes are then assigned the force equal to average of these weights: $\gamma_{ij} = (\gamma_i + \gamma_j)/2$. Nodes that get too close to the node i_M carrying the myosin spot are absorbed, with their area weight dA_j added to the myosin spot, effectively increasing the drag between this node and substrate. Thus, over time, all the area weight (~actin density) should converge to the myosin spot node (which itself will move with time).

For simplicity, in the simulations, all myosin spots are identical and scale as γ_0 divided by the number of the initial spots (this way, the total myosin strength is approximately constant in cases considered). However, see additional notes below about the myosin stresses.

Comments on the network's rheology

The internal material properties of the network are not known in detail, and in principle, on the relevant time scale longer than minutes, the network could be purely viscous. However, when we simulated the network as a compressible viscous fluid, the resultant velocity fields for a given myosin distribution were different from the observations. Though the boundary conditions and inherent boundary shape would result in flow toward the center in homogeneous patterns, the relative magnitudes of local network flow (and thus resultant deformation) close to the myosin spot and far from it were different from the observations. Most importantly, flow between myosin spots was not quiescent as observed in experiments (see Figure. 3). On the other hand, a purely elastic network, of course, only deforms partially and never compacts to the center. So, a viscoelastic description is necessary.

Lastly, having a network more resistant to stretching works best because network compaction close to myosin spots is more effective than if resistance to compression is equally high. More importantly, we know resistance to stretch is required for capturing the observed lack of flow between myosin spots and having a higher resistance to stretch than compression best captures the ratio of flow magnitudes between spots versus close to spots being much smaller than 1. All these reasons and trial simulations with other possible rheologies provided rationale for the model choice.

Parameters

Non-dimensional model parameters are listed in this table:

Parameter	Non-dimensional value
Elastic modulus λ_E	50
Discretization length h_x *(approximate starting link length*)	$1/16 \ = \ 0.0625$
Stretch spring constant $k_{ij} = \frac{8\lambda_E}{3\ell_{ij}^0}\left(\frac{dA_i + dA_j}{2}\right)$	Initialized as $\sim \ 8$ for internal nodes, between $\sim$ 3 and ~ 5 for border nodes, when using the above λ_E and h_x
Ratio of compression to stretch spring constant r_k	0.15
Relaxation time $1/r$	1/2
Maximum contractile force γ_0	2.0
Contraction range (gaussian width σ_m)	0.05
Lipid drag coefficient ζ_1	300
Glass drag coefficient ζ_2	850
Timestep dt	0.0001

These choices are justified as follows. The non-dimensional length scale is such that one length unit corresponded to the width of the pattern (square width, 60 μm, or disk diameter, 70 μm, which is also used for the rectangle case). The initial rest length of the springs is set to be roughly equal to the initial discretization length which is 1/16th of the non-dimensional length unit. To operate with forces on the order of unity, it is convenient to have the compression spring constant on the order of unity. We found that this is the case if we choose the non-dimensional value for the elastic modulus equal to 50. The ratio k_{ij}/ℓ_{ij}^0 was kept constant throughout the simulations. The stretch spring constant must be at least a few fold greater than the compression spring constant for the global stress propagation in the network, but not more than an order of magnitude greater to avoid numerical instabilities associated with occasional local remeshing which produces relaxed links. We found that the compression / stretch spring constant ratio 0.15 worked well in combination with compression spring constants initialized to be at least ~ 0.5. We chose the maximal contractile force to be on the order of unity; then, at the observed strains of the network and chosen relaxation rate, respective internal elastic forces are approximately a magnitude smaller than the local myosin contractile forces, and so the local contractile behavior is predominantly the balance between the myosin active force and the friction between the network and substrate. To keep the myosin contraction local and highly concentrated in spots, we chose the contraction range to be on the order of the average node-to-node distance. We chose the order of magnitude of the non-dimensional viscous drag (per small area around the node) coefficients for this friction in the range from 100 to 1000;

given the chosen discretization size h_x, this means the product of drag and area weight ζdA_i on a node is usually on the $O(0.1 - 1.0)$ (so, of a comparable magnitude to forces considered). The drag coefficient indirectly determines the time unit (because the force and length units are already chosen, and viscous drag's dimension contains units of force, length and time), so choosing a larger non-dimensional viscous drag, given the choice of timestep dt, allows for the contraction to proceed slowly enough to avoid numerical problems but not so slowly that computation runtime is exceedingly high. The time step was necessitated by considerations of numerical stability. With these parameters, the network compaction (on lipid) was generally completed in ~ 10 non-dimensional time units (approximately 13 non-dimensional time units on the square pattern), which we took to correspond to 23 min of biological time to match the measurements. The links' characteristic relaxation time was chosen to be on the order of one non-dimensional time unit to be much shorter than the duration of the network compaction, in order for the long-term network behavior to be more viscous than elastic, but not smaller than one non-dimensional time unit in order for the elastic stresses not to become too weak too fast, which would make the contraction very local. Additionally, the relaxation time cannot be so short that stretched links are instantly relaxed, which would mean the disproportionate stretch to compression response would not be evident. Lastly, the ratio of the glass to lipid viscous drags was determined by fitting the ratio of the resulting rates of area decrease for various choices of viscous drag coefficients, such that the relative rates of area decrease match experimental quantitative estimates.

Numerical implementation

Initialization

Given a chosen domain shape (square, disk, rectangle), the domain is coarse-grained using the distmesh package (5) which utilizes an algorithm which employs Delaunay triangulation to generate a network of points with links of $\approx h_x$ equal length. The initial links' lengths are assigned as the starting rest lengths, such that initially the network has no passive internal stresses, and if no external or active forces are applied then the material does not deform.

Time-stepping

At each timestep, links are assigned their active contractile tensions γ_{ij} based on the sum of myosin spot contributions given by Eq. (6). The elastic forces are calculated, and node positions $\boldsymbol{x_i(t)}$ are updated by taking a Forward Euler step of Eq. (4). Simultaneously, the link rest lengths ℓ_{ij}^0 are updated also with a Forward Euler step of Eq. (5), and the spring stiffnesses are accordingly adjusted as previously described.

Myosin spot node absorption

We analyzed the quantity of myosin in foci compared to the total intensity of myosin (not shown). During the contraction phase, ratio of myosin in foci to total quantity of myosin is high and remains close to one over time. This is why in simulations we focused on the myosin localized within foci.

The effect of a myosin spot is primarily localized within a $2\sigma_M$ distance of node i_M. This parameter σ_M is chosen to be comparable to the initial node-node distance h_x. When a node j that is a first neighbor of the myosin spot and within a $h_x/6$ distance from the spot, node j is "absorbed" by node i_M such that $dA_{i_M} \rightarrow dA_{i_M} + dA_j$. This absorption distance is chosen such that there is little difference

in the calculation of contractile forces γ_{ij} locally with or without node j. The myosin spot and other remaining first neighbors of node j become connected with a local Delaunay triangulation, assigning the new links rest lengths ℓ_{ij}^0 which are relaxed ($= \ell_{ij}$) and spring constants k_{ij} approximately equal to that of the lost edges. This choice of ℓ_{ij}^0 and k_{ij} for the new edges ensures any transient responses due to remeshing are minimized – assigning the rest lengths and spring constants differently from this would be relatively inconsequential, since the contractile forces γ_{ij} on links close to the myosin spot is the dominant internal force for the nodes.

Remeshing and extra numerical conditions

It is necessary to add additional implementation measures to prevent unphysical behaviors (for example, with strong enough non-uniform compressive loads the network could overlap over itself). Since there is long-time viscous behavior, it is appropriate to occasionally perform local remeshing of the network to delete and/or add new links to prevent these behaviors. We implement two kinds of local remeshing: remeshing of low-quality triangles (as determined by distmesh function simpqual) and remeshing of cusped boundary points.

If the quality of a triangle, which ranges from 0 to 1, is < 0.05 then this triangle and all its nodes' first neighbors are remeshed according to Delaunay triangulation rules. No links which overlap the rest of the triangulation are added. These new edges have rest lengths ℓ_{ij}^0 which are relaxed with spring constants k_{ij} equal to the average lost edge spring constant times the ratio of the new rest length to average old edge rest lengths. This ensures that the network does weaken due to local remeshing, while also minimizing any transient response due to remeshing. The low-quality triangle remeshing occurs until at most 40% of the network becomes localized at the myosin spots, which is generally when most of the network has contracted to a small region and nearly all triangles become low quality.

At initialization, the boundary nodes of the network are known. Considering these nodes as forming a polygon, the exterior angles are tracked with time. If an exterior angle drops below $100°$, as typically occurs when a piece of the domain boundary approaches a myosin spot, the associated exterior node is removed and its area weight is redistributed to its neighbors equally. The node's first neighbors are reconnected according to Delaunay triangulation rules, proceeding as described above for low quality triangles. The boundary remeshing occurs until at most 80% of the network becomes localized at the myosin spots, after which very few boundary nodes remain and the network is highly compacted so remeshing is unnecessary.

In the rare instances that a node disconnects from the bulk network due to these local remeshing rules, it is removed from the system and its area weight is redistributed to its closest neighbors. Generally, this occurs rarely and in regions when nodes are densely packed, so any choice of node weight distribution does not significantly affect even the quantitative results.

Finally, if a node pair has link distance $\ell_{ij} < h_x/11$, we assume the spring constant k_{ij} becomes infinite so that the link cannot compress any further. We found that a condition of this form is necessary to avoid unphysical behaviors close to the myosin spots, where contraction is very high. Effectively, this condition ensures that such node pairs move as a unit together until one or both are absorbed by a myosin spot.

Location of the network convergence point

On a uniform pattern, the network compacts to the centroid.

At every node i, the internal forces (active contraction, elastic responses, etc.) are balanced with the external friction force:

$$\boldsymbol{F_i^{int}}(\boldsymbol{x}_i) \;=\; \zeta(\boldsymbol{x}_i)\frac{d\boldsymbol{x}_i}{dt}dA_i \qquad (7)$$

where $\boldsymbol{x}_i(t)$ is the position of the node i over time and dA_i is the area weight, a proxy for the initial actin density carried by the node. Note that we presume the actin density to be fixed and advected on the nodes. For simplicity, let's assume that all nodes carry the same initial actin mass, taking $dA_i = 1$ in Eq. (7). The internal forces over all nodes must sum to zero according to Newton's third law (as an internal force on node i from node j is equal and opposite to the internal force on node j from node i). This means that

$$\sum_i \boldsymbol{F_i^{int}}(\boldsymbol{x}_i) \;= \mathbf{0}$$

Necessarily, by applying this equality to Eq. (7) we then have:

$$\textstyle\sum_i \zeta(\boldsymbol{x}_i)\frac{d\boldsymbol{x}_i}{dt} = \mathbf{0} \qquad (8)$$

First, consider Eq. (8) in the case of a homogeneous pattern where $\zeta(\boldsymbol{x}) = \zeta$, a constant. We can swap the time derivative with the summation,

$$\frac{d}{dt}\sum_i \zeta\, \boldsymbol{x}_i \;= \mathbf{0}$$

then time integrating gives us

$$\textstyle\sum_i \zeta\, \boldsymbol{x}_i \;= \boldsymbol{const.}$$

Equivalently

$$\textstyle\sum_i \zeta\, \boldsymbol{x}_i / \sum_i \zeta = \boldsymbol{const.} \qquad (9)$$

Notice that the left-hand-side of Eq. (9) is a center-of-mass calculation, except mass density is replaced by viscous drag. More generally when drag may depend on node position, we refer to summations of the form

$$\textstyle\sum_i \zeta(\boldsymbol{x}_i)\, \boldsymbol{x}_i / \sum_i \zeta(\boldsymbol{x}_i) \qquad (10)$$

as the instantaneous center-of-drag of the system.

Eq. (9) then states that at any stage of the contraction, the center-of-drag of the network does not shift. Necessarily, the compaction point at which all $\boldsymbol{x}_i$ node positions converge is exactly the center-of-drag at the final time, which by Eq. (9) equals the center-of-drag at the onset. Though the node positions $\boldsymbol{x}_i = \boldsymbol{x}_i(t)$ are time dependent and may vary based on myosin distribution, we can easily compute the center-

of-drag at the contraction onset. Since we are dealing with the especially straightforward case of a homogeneous pattern, this center-of-drag coincides with the centroid: the geometric center of the chosen domain. This is exactly the convergence point we observe in the homogeneous square, disk, and rectangle cases.

Now, suppose that the pattern is not homogeneous, i.e. $\zeta(\boldsymbol{x})$ depends on the position $\boldsymbol{x}_i$ of a node. It is easiest to discuss this in the context of viewing the network as a continuum, continuing in Lagrangian coordinates – meaning $\boldsymbol{x} = \boldsymbol{x}(\boldsymbol{x_0}, t)$ where $\boldsymbol{x_0}$ is the initial position in the reference configuration. The equivalents to Eq. (7) and (8) are:

$$\boldsymbol{F^{int}}(\boldsymbol{x}) = \zeta(\boldsymbol{x})\frac{d\boldsymbol{x}}{dt} \qquad (7')$$

$$\int \zeta(\boldsymbol{x})\frac{d\boldsymbol{x}}{dt}\, dA_0 = 0 \qquad (8')$$

Here $\boldsymbol{F^{int}}(\boldsymbol{x})$ is the force density. In the context of patterns which are not homogeneous, we seek to understand how the center of drag

$$\boldsymbol{c}_D = \int \zeta(\boldsymbol{x})\boldsymbol{x}\, dA_0 \,/ \int \zeta(\boldsymbol{x})\, dA_0 \qquad (11)$$

changes with time. Note that Eq. (11) is the continuous analogue of Eq. (10). The final position of the center of drag $\boldsymbol{c}_D$ must necessarily coincide with the convergence point of the nodes. Taking the time derivative of Eq. (11), we have

$$\frac{d}{dt}(\boldsymbol{c}_D) = \frac{d}{dt}\left(\int \zeta(\boldsymbol{x})\boldsymbol{x}\, dA_0\right)\frac{1}{\int \zeta(\boldsymbol{x}) dA_0} + \int \zeta(\boldsymbol{x})\boldsymbol{x}\, dA_0\left(-\frac{\frac{d}{dt}\left(\int \zeta(\boldsymbol{x}) dA_0\right)}{\left(\int \zeta(\boldsymbol{x}) dA_0\right)^2}\right)$$

$$= \frac{1}{\int \zeta(\boldsymbol{x}) dA_0}\left(\int \zeta(\boldsymbol{x})\frac{d\boldsymbol{x}}{dt}\, dA_0 + \int \nabla\zeta \cdot \frac{d\boldsymbol{x}}{dt}\,\boldsymbol{x}\, dA_0 - \frac{\int \zeta(\boldsymbol{x})\boldsymbol{x}\, dA_0}{\int \zeta(\boldsymbol{x}) dA_0}\int \nabla\zeta \cdot \frac{d\boldsymbol{x}}{dt}\, dA_0\right) \qquad (12)$$

The first term in Eq. (12) is identically zero by Eq. (8'), so we have that the center of drag changes with time as:

$$\frac{d}{dt}(\boldsymbol{c}_D) = \left(\int \nabla\zeta \cdot \frac{d\boldsymbol{x}}{dt}\,\boldsymbol{x}\, dA_0 - \boldsymbol{c}_D \int \nabla\zeta \cdot \frac{d\boldsymbol{x}}{dt}\, dA_0\right)\Big/ \int \zeta(\boldsymbol{x}) dA_0 \quad (13)$$

In particular, notice the relevance of the inner product of the change in drag with the velocity; this term $\nabla\zeta \cdot \frac{d\boldsymbol{x}}{dt}$ is nonzero when there is flow parallel to the direction of change in drag.

To gain further intuition as to the meaning of Eq (13), let us consider the case of a heterogeneous rectangular domain, where

$$\zeta(x, y) = \begin{cases} \zeta_1, & x < 0 \\ \zeta_2, & x \geq 0 \end{cases} = \Delta\zeta\, H(x) + \zeta_1$$

Let us choose $\Delta\zeta = \zeta_2 - \zeta_1 > 0$ (as is consistent with a lipid-drag left-right divide). Note that $H(x)$ is the Heaviside step function. Then, in this pattern case, the gradient of drag is simply

$$\nabla\zeta = <\Delta\zeta\, \delta(x), 0>$$

Then, letting $\frac{d\boldsymbol{x}}{dt} = <u, v>$, Eq. (13) becomes

$$\frac{d}{dt}(\boldsymbol{c}_D) = \frac{1}{\int \zeta(\boldsymbol{x}) dA_0}\left(\int \Delta\zeta\, \delta(\mathrm{x})\, u\, \boldsymbol{x}\, dA_0 - \boldsymbol{c}_D \int \Delta\zeta\, \delta(\mathrm{x})\, u\, dA_0\right) \quad (14)$$

Because of the delta function in x, integrals are only nonzero when considering reference positions $\boldsymbol{x_0}$ such that $x = 0$ (i.e. we only integrate over particles which currently at time t live on the lipid-drag divide). Let us call the set of reference positions who's current x position is $x = 0$ the set $S(t) = \{\boldsymbol{x_0} \text{ such that } x(\boldsymbol{x_0}) = 0\}$. Looking more closely at the time evolution of $\boldsymbol{c}_D \cdot x$, since that is the direction with asymmetry, we have

$$\frac{d}{dt}(\boldsymbol{c}_D \cdot \hat{\boldsymbol{x}}) = \frac{-\boldsymbol{c}_D \cdot \hat{\boldsymbol{x}}}{\int \zeta(\boldsymbol{x}) dA_0} \int_{S(t)} \Delta\zeta \, u \, dA_0 \quad (15).$$

Now, remember $\Delta\zeta > 0$ and we can assume that the horizontal flow u along the boundary $x = 0$ is nearly always to the right, i.e. $u > 0$. The total drag at any moment in time, $\int \zeta(\boldsymbol{x}) dA_0$, is also strictly positive. Finally, the x coordinate of the center of drag $\boldsymbol{c}_D \cdot \hat{\boldsymbol{x}}$ is expected to be preferentially in the $x > 0$ regime, since the $x > 0$ side has a higher drag coefficient than the $x < 0$ side of the regime. All this put together suggests that, in fact,

$$\frac{d}{dt}(\boldsymbol{c}_D \cdot \hat{\boldsymbol{x}}) < 0 \qquad (16)$$

for the majority of time t during contraction. Eq. (16) means we expect the x coordinate of the center of drag $\boldsymbol{c}_D$ to shift away from its $t = 0$ value in the direction of the lipid-glass divide where the drag changes.

Given the simple case of a heterogeneous domain, we have gained valuable intuition regarding Eq. (13), which more generally describes how the center of drag changes with time. Eq. (13) tells us that there are two primary factors: one, the "drag flux" associated with the flow in the direction of changes in drag coefficient spatially and two, the location of these spatial changes in the drag coefficient (as is suggested by first term $\int \nabla\zeta \cdot \frac{d\boldsymbol{x}}{dt} \, \boldsymbol{x} \, dA_0$).
More generally, in the heterogeneous case, the movement of nodes into regimes of higher drag penalizes the center of drag preferentially in the direction of this change.

Estimate of the convergence point coordinates on the heterogeneous pattern

We have just shown that the cross-over of the network into regions of higher drag penalizes the center of drag towards the lipid-drag divide, but what is less clear is the extent to which the center of drag moves from its starting location at time $t = 0$.

Let us first calculate the initial center of drag $\boldsymbol{c}_D(t = 0)$, as in Eq. (11), in all considered experimental cases. This initial position should be an upper bound of sorts on the final $\boldsymbol{c}_D$ after compaction. We consider the square $[-0.5,0.5]^2$, rectangle $[-0.75,0.75] \times [-0.25,0.25]$, and disk centered at 0 with radius 0.5 (here, 1 is the non-dimensional length unit). Let the lipid drag coefficient be ζ_1 and the glass drag coefficient be ζ_2. Then,

$$\boldsymbol{c}_D(t = 0) = < 0.25 - \frac{1}{2}\left(1 + \frac{\zeta_2}{\zeta_1}\right)^{-1}, 0 > \qquad \text{[heterogenous square]}$$

$$\boldsymbol{c}_D(t = 0) = < \frac{1}{3}\left(\frac{1+2\,\zeta_2/\zeta_1}{1+\zeta_2/\zeta_1}\right) - 0.5, \frac{1}{3}\left(\frac{1+2\,\zeta_2/\zeta_1}{1+\zeta_2/\zeta_1}\right) - 0.5 > \qquad \text{[diagonal square]}$$

$$\boldsymbol{c}_D(t = 0) = < 0.375 - 0.75\left(1 + \frac{\zeta_2}{\zeta_1}\right)^{-1}, 0 > \qquad \text{[heterogenous rectangle]}$$

$$\boldsymbol{c}_D(t=0) =< \frac{1}{2}\left(\frac{1+2\,\zeta_2/\zeta_1}{1+\zeta_2/\zeta_1}\right) - 0.75, \frac{1}{6}\left(\frac{1+2\,\zeta_2/\zeta_1}{1+\zeta_2/\zeta_1}\right) - 0.25 > \quad \text{[diagonal rectangle]}$$

$$\boldsymbol{c}_D(t=0) =< \frac{2}{3\pi}\left(\frac{\zeta_2/\zeta_1 - 1}{\zeta_2/\zeta_1 + 1}\right), 0 > \quad \text{[heterogenous disk]}$$

In all these cases, for times $t > 0$ we expect $\boldsymbol{c}_D$ to shift in the direction of the lipid-glass divide. Without additional factors in the dynamics, this puts a hard limit on the depth of the contraction point in the glass regime.

Since generally lipid surfaces tend to contract before drag surfaces, let us consider the special case where the lipid portion of the domain has entirely contracted to the lipid-glass boundary. There are experimental observations (Figure 4) that suggest this special case to be almost true since the lipid and glass surfaces have different lag times before contraction. Note that if the drag part of the network is fixed (effectively with a very large drag coefficient) while the lipid part is contracting, up until the glass part starts contracting the center of drag $\boldsymbol{c}_D$ will be farther into the glass portion of the domain than as calculated above. So even if ζ_2/ζ_1 is close to 1, the time delay in contraction inherently shifts the drag coefficient away from the centroid.

For this special case, let us presume that the lipid part of the network contracts to the drag boundary and that it is distributed along this boundary as if contractile flow was net perpendicular to the boundary. In the square and glass cases, this would yield a distribution of the compacted lipid portion which is symmetric around the center of the domain. Once the lipid portion of the network has completely contracted to the boundary and if we presume the glass portion of the network is uniform, then we can apply the center of drag argument for homogeneous domains, as in Eq. (9), as all of the network experiences the same drag coefficient. Note that, presuming the lipid contracts fully to the boundary first, then *regardless of the choice of drag coefficients* the convergence point of the network must be

$$\boldsymbol{c}_D^*(t_{final}) =< 0.125, 0.0 > \quad \text{[heterogenous square]}$$

$$\boldsymbol{c}_D^*(t_{final}) =< 7/12, 7/12 > \approx < 0.083, 0.083 > \quad \text{[diagonal square]}$$

$$\boldsymbol{c}_D^*(t_{final}) =< 0.1875, 0.0 > \quad \text{[heterogenous rectangle]}$$

$$\boldsymbol{c}_D^*(t_{final}) = < 0.025, 0.075 > \quad \text{[diagonal rectangle]}$$

$$\boldsymbol{c}_D^*(t_{final}) =< 1/3\pi, 0 > \approx < 0.10, 0.0 > \quad \text{[heterogenous disk]}$$

Note that excluding the rectangular diagonal case[1], $\boldsymbol{c}_D^*(t_{final})$and $\boldsymbol{c}_D(t=0)$ are identical for a glass/lipid ratio of $\zeta_2/\zeta_1 = 3$. Below this ratio, $\boldsymbol{c}_D(t=0) < \boldsymbol{c}_D^*(t_{final})$ and above this ratio $\boldsymbol{c}_D(t=0) > \boldsymbol{c}_D^*(t_{final})$. Essentially, this tells us that if the glass/lipid drag ratio is $\zeta_2/\zeta_1 < 3$ then a time delay in contraction pushes the final contraction position closer to $\boldsymbol{c}_D^*(t_{final})$, beyond $\boldsymbol{c}_D(t=0)$.

[1] In the diagonal rectangle case, we assumed the flow was perpendicular to the drag boundary. This preferentially places the lipid portion of the network to be primarily in the $x < 0$ part of the domain, while the glass portion is primarily in the $x > 0$ part of the domain due to the aspect ratio. This affects the final position be close to $x = 0$ but this is not necessarily what we would expect the effect of flow through the boundary to be on $\boldsymbol{c}_D(t > 0)$.

If the glass/lipid drag ratio is $\zeta_2/\zeta_1 > 3$, $\boldsymbol{c}_D^*(t_{final})$ should still be a rough estimate of the final contraction position, since the glass portion of the network is mostly stationary as the lipid part contracts so we can reasonably expect the lipid portion of the network to contract to the boundary before significant deformation of the glass part has occurred.

In sum, with our understanding of how the center of drag changes over time (Eq. (12)) and the estimated final positions $\boldsymbol{c}_D^*(t_{final})$ for the special case associated with a time delay, generally we expect that the final position be close to $\boldsymbol{c}_D^*(t_{final})$, except in the diagonal rectangular case where the predicted final position is more likely to be point along the line from the drag boundary to the initial center of drag $\boldsymbol{c}_D(t = 0)$.

Why theory and simulation underestimate the distance between the convergence point and centroid on the heterogeneous pattern

If the domain is heterogenous (lipid/glass), the numerical simulation predictions for the convergence points are slightly lower than the final analytical estimates of the previous section. This simulation underestimation is partly because the simulations rarely reach the extreme case of the lipid side fully contracting to the boundary (and there is always some minimal error associated with discretization and implementation simplifications). But even these analytical estimates of the distance between the convergence point and centroid of the pattern are slightly lower than the *average* experimentally measured distance (the lowest measured distances compare nicely to the computed ones). There are likely two reasons for the underestimation by the model. First, in the model we neglected network disassembly, but some disassembly likely does take place. Then, it is likely that the part of the network that is initially on lipid will start disassembling earlier because it started contracting earlier. This would give a lower 'weight' to the drag of the network on the lipid part, shifting the center of the drag deeper into the glass part. Second, the retraction fibers, clearly visible in the final stages of the network compaction, could be effectively pulled into the final large myosin aggregate at the focal point of these fibers' aster. The aggregate's position is then biased by the effective friction between these fibers and substrate. Under some simple assumptions, this bias is toward the center of the glass part of the pattern.

Centering with acceleration

Numerical simulations predict velocity of the myosin spots directed toward the centroid of the homogeneous pattern, and roughly toward the center-of-drag of the heterogeneous pattern, with speed gradually slowing down near the convergence point. The direction is predicted correctly, but the experimentally observed speed increases near the convergence point. The simple explanation of this phenomenon is: First, we observe that the total myosin amount in the myosin spots increases substantially during the contraction. From the model, the spots' speeds accelerate with the increase of the myosin strength, which is proportional to the myosin density. Second, the network likely undergoes partial disassembly during the contraction. Because of that, the friction force is likely to gradually decrease, also serving to accelerate the contraction.

Square pattern contracts faster than disc pattern

This observation can be explained by the model providing the following two assumptions are true: the average amount of myosin per spot does not depend on the number of spots (and so the total amount of myosin in all spots increases with the spot number), and the average number of spots per pattern is greater on a square than on a disc. The second of these assumptions is true, based on the

observations. The reason for that is likely that the initial myosin spots preferentially appear in the corners of the pattern because initial myosin condensation is accelerated in the corner: distributed contraction is faster near the outwardly curving boundary, as previously published simulations predict (6). We also saw in our simulations that at the initial stage of contraction, each spot generates a roughly constant rate of the area decrease, and as far as the spots are far from each other, the effect is additive. Then, if the first assumption is correct, the net rate of the area reduction scales with the number of spots, explaining why the rate of the area decrease on the square pattern is greater than that on the disc pattern.

Why centering is less coordinated on glass than on lipid

There are two factors that make the contraction less coordinated on glass compared to lipid, one of these factors is apparent from the experiment, another – hypothesized. The first factor is suggested by the much more symmetric assembly of the myosin aggregates (spots) on lipid patterns. We observed that on the glass square pattern, the initial distribution of the myosin spots is most often asymmetric (for example, there is one spot in one of the corners, or two spots in the adjacent corners). In those cases, due to the subtle factors not included into the model, like contraction-dependent partial network disassembly and/or some dependence of the effective friction on the history of drag across local patches of the surface, these factors would translate into asymmetries of the contractions violating the theorem of the compaction to the centroid. In other words, the more asymmetric the initial myosin spot distribution is, the greater the shift from the center of the pattern is for the convergence point, which is the case on the glass patterns. On the lipid square patterns, the initial myosin spots are distributed more symmetrically, like four spots in all four corners. In this case, the contraction must be symmetric, converging exactly to the center.

Of course, this raises another question – why the myosin spots arise less symmetrically on glass. This could be explained, hypothetically, by the difference in friction: large myosin aggregates assemble on dense clusters of nascent actin network. On lipid, where small actin network fragments are more mobile, the nascent clusters spread more homogeneously seeding multiple network islands that become assembling templates for myosin. On glass, the autocatalytic nature of branching, due to a limited mobility, often leads to dominant growth of a single actin cluster, and thus to a single myosin aggregate.

The second factor could be due to a gripping-slipping threshold of friction. The longer lag phase before the contraction starts could originate, in part, from a force threshold needed to overcome the friction. When the myosin-powered force is sufficient to break these bonds, the network does not grip the glass anymore, and the viscous slipping ensues. Such breaking has a stochastic character, which was demonstrated by studies on adhesion clutch, and random variations of the gripping-slipping transition across the glass pattern could contribute to the less coordinated contraction.

Supporting Figures

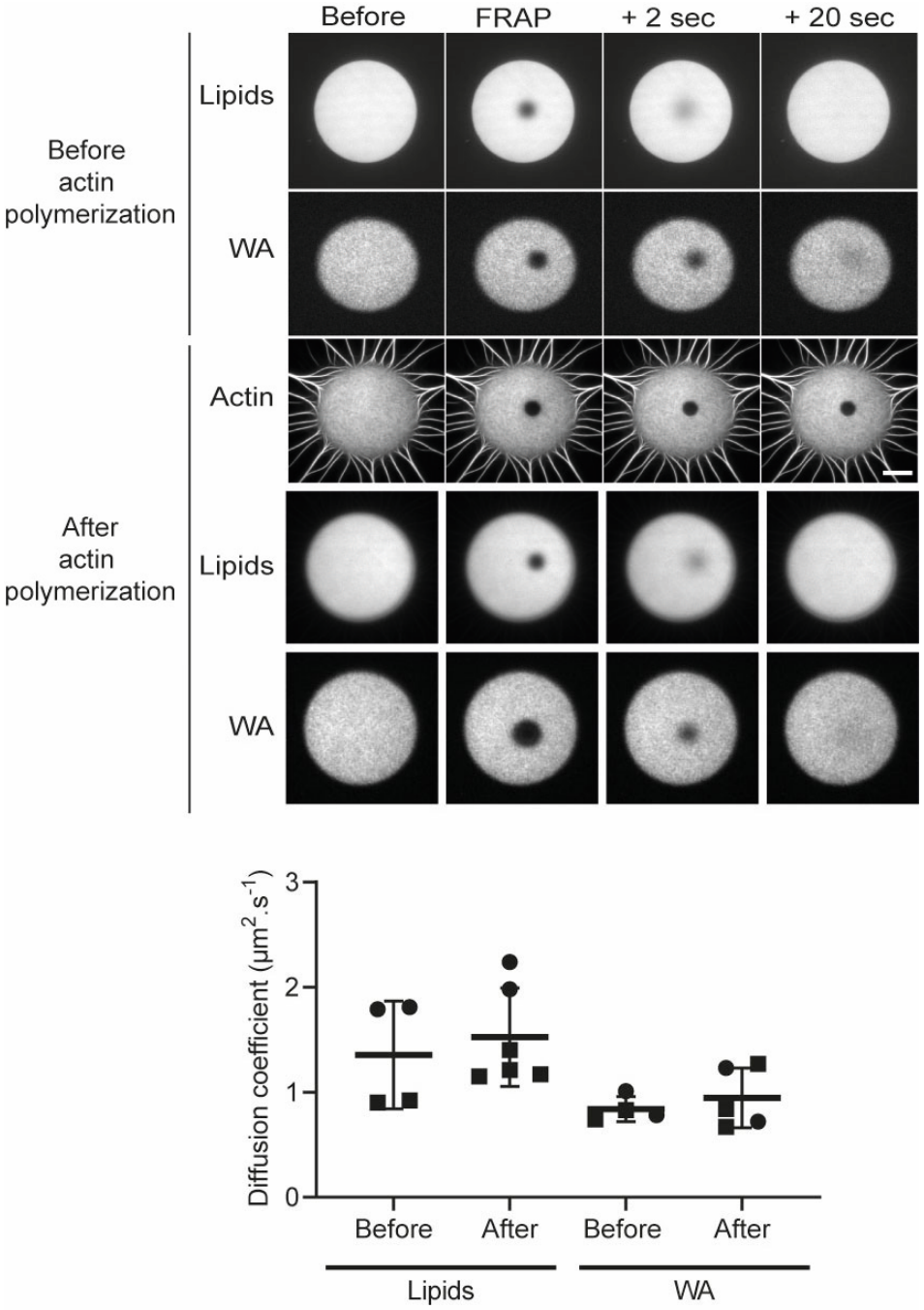

Supporting Figure 1. Lipids and WA diffusion are unchanged before and after actin polymerization. Top: Snapshots of FRAP experiment on lipids, WA and actin before and after actin polymerization. Bottom: estimation of diffusion coefficients for the different experimental conditions shown above. N = 2. Lipids, Before: n = 4. Lipids, After: n = 6. WA, Before: n = 4. WA, After: n = 5. (N : independent experiments, n: number of patterns on which FRAP was done, the different symbols on the figure represent the independent experiments. Mean and standard deviation are superimposed).

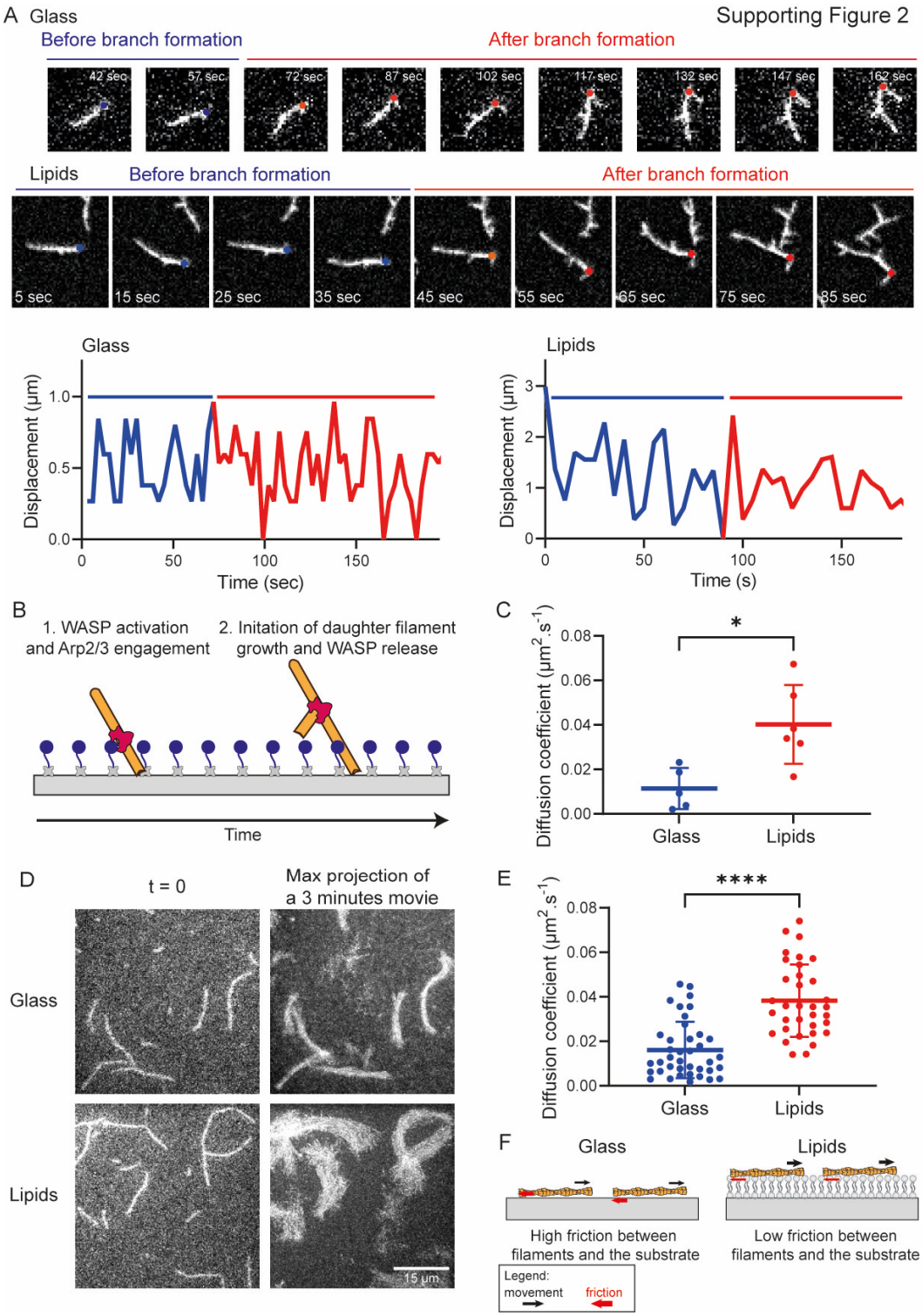

Supporting Figure 2. Friction origin is due to the interaction of actin filaments with the substrate. A. (Top) Snapshots of branch formation on glass or lipid patterns. The blue part corresponds to the filament before the branch formation and the red part, after the branch formation. (Bottom) Displacement of the filament before and after branch formation for the glass and lipid substrates. **B.** Scheme of the WASP activation and release for the daughter filament growth. **C.** Diffusion coefficient estimation for the branches diffusion on glass or on

lipid micropatterns. (N = 1, n = 5 filaments on glass, n = 6 filaments on lipids. Mann-Whitney statistics: p-value = 0.0173 *) **D.** Snapshots and maximum projection of a 3 minutes movie for single filaments on glass or lipid micropatterns. **E.** Diffusion coefficient estimation for the single filaments diffusion on glass or on lipid micropatterns. (Glass: N = 4, n = 40 filaments. Lipids: N = 2, 34 filaments. Mann-Whitney statistics: p-value<0.0001****). **F.** Scheme of the interaction between actin filaments and glass or lipid substrates, leading to high or low frictions.

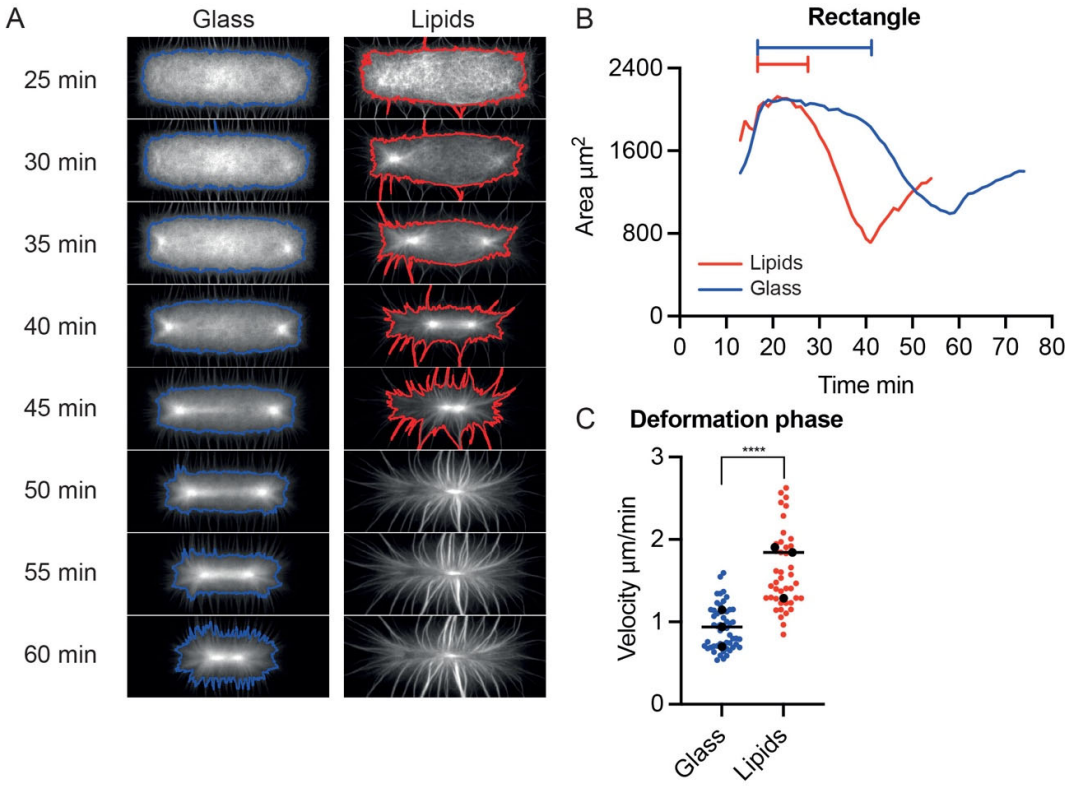

Supporting Figure 3. Contraction of rectangle-shaped actin network on glass or lipid micropatterns.

A. Time-lapse imaging of actin network contraction on a glass or lipid rectangle (L=104 µm, l=34 µm) micropattern. Line (Blue for glass, Red for lipids) correspond to the contours of the actin network (see methods). Biochemical conditions: On glass micropattern, WA = 1 µM; on lipid micropattern: WA = 1 nM. Actin 1µM, Human Profilin 3 µM, Arp2/3 complex 25 nM, Myosin VI 14 nM. **B.** Measured actin area as a function of time for the lipid (red) or glass (red) conditions. **C.** Velocity of the phase contraction phase for the lipid or glass conditions on rectangle micropattern. Data are represented with a superplot. Rectangle Glass n=52-N=3-*median* =0.9089, Rectangle Lipids n=68-N=4-*median* =1.474. Mann-Whitney Statistics: Rectangle Glass/Rectangle Lipids *p* value≤0.0001 ****.

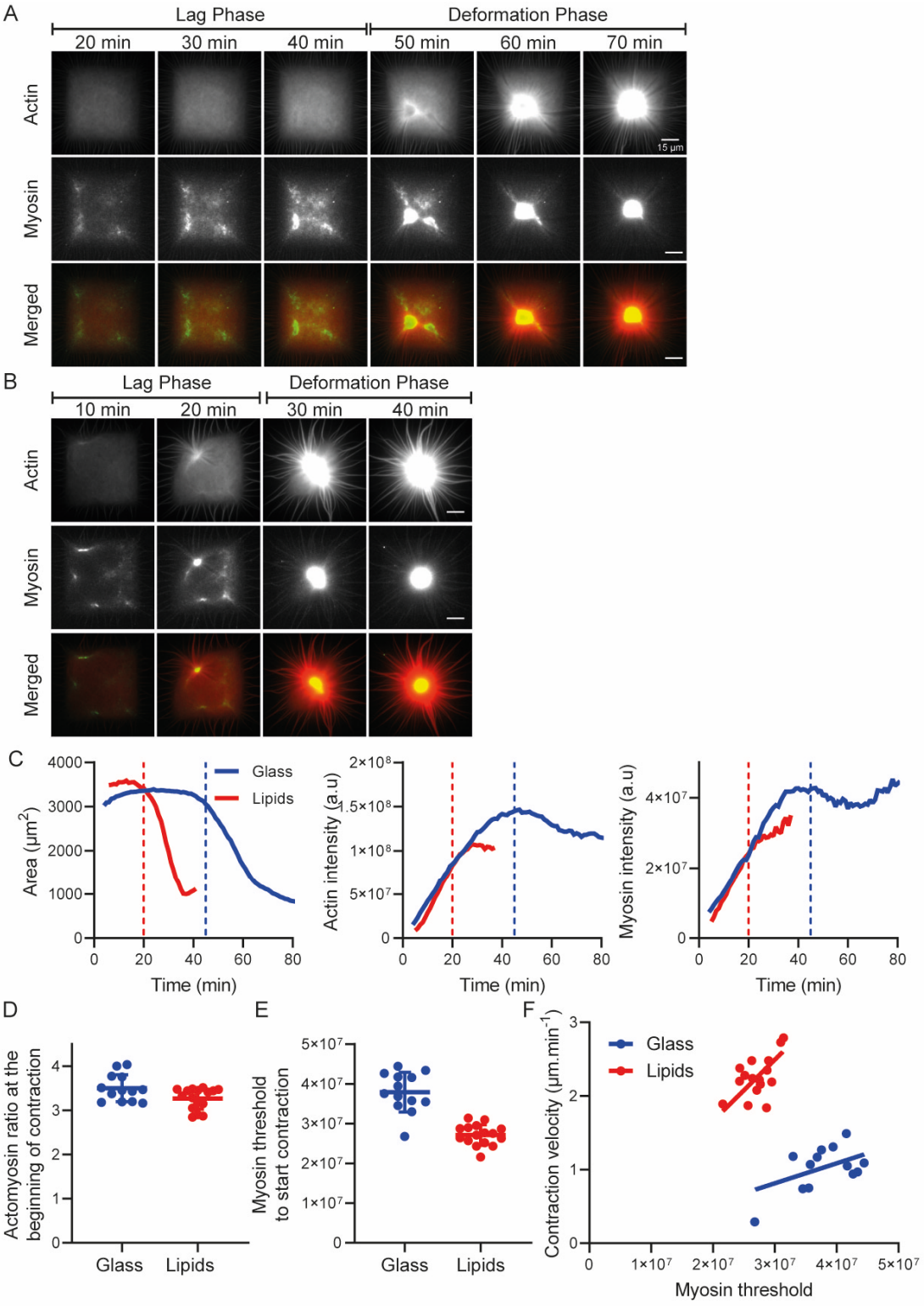

Supporting Figure 4. Accumulation of actin and myosin during the lag phase leads to a lower myosin threshold to start contraction on lipids micropatterns. A,B. Snapshots of a micropattern contracting on glass (A) or lipid (B) substrate. **C.** Area, Actin intensity and Myosin intensity for the two examples shown above. The dashed vertical lines indicate the beginning

of the contraction on glass substrate (blue line) or lipid substrate (red line). **D.** Actomyosin ratio at the beginning of the contraction on glass or lipid substrate. **E.** Myosin threshold to start the contraction on glass or lipid substrate. **F.** Correlation between the contraction velocity and the myosin threshold at the beginning of the contraction. Line represents the linear regression on the individual points. Glass: slope = $2.71.10^{-8}$. Lipids: slope = $8.31.10^{-8}$. Individual point represent single patterns. Mean and standard deviation are superimposed.

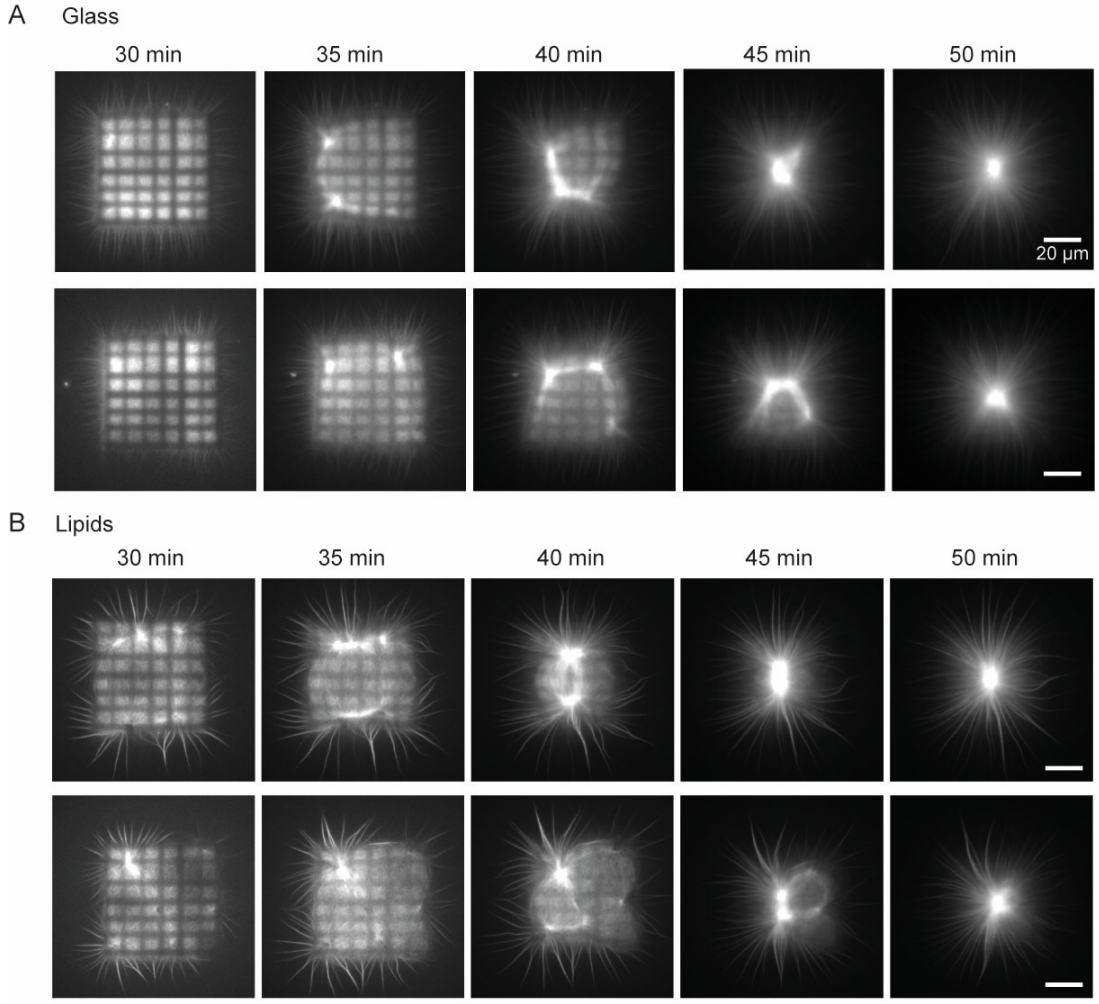

Supporting Figure 5. Contraction of actin network with a photobleached grid. A. Two examples of photobleached grids and the following contraction of the actin network on glass micropatterns. **B.** Two examples of photobleached grids and the following contraction of the actin network on lipids micropatterns.

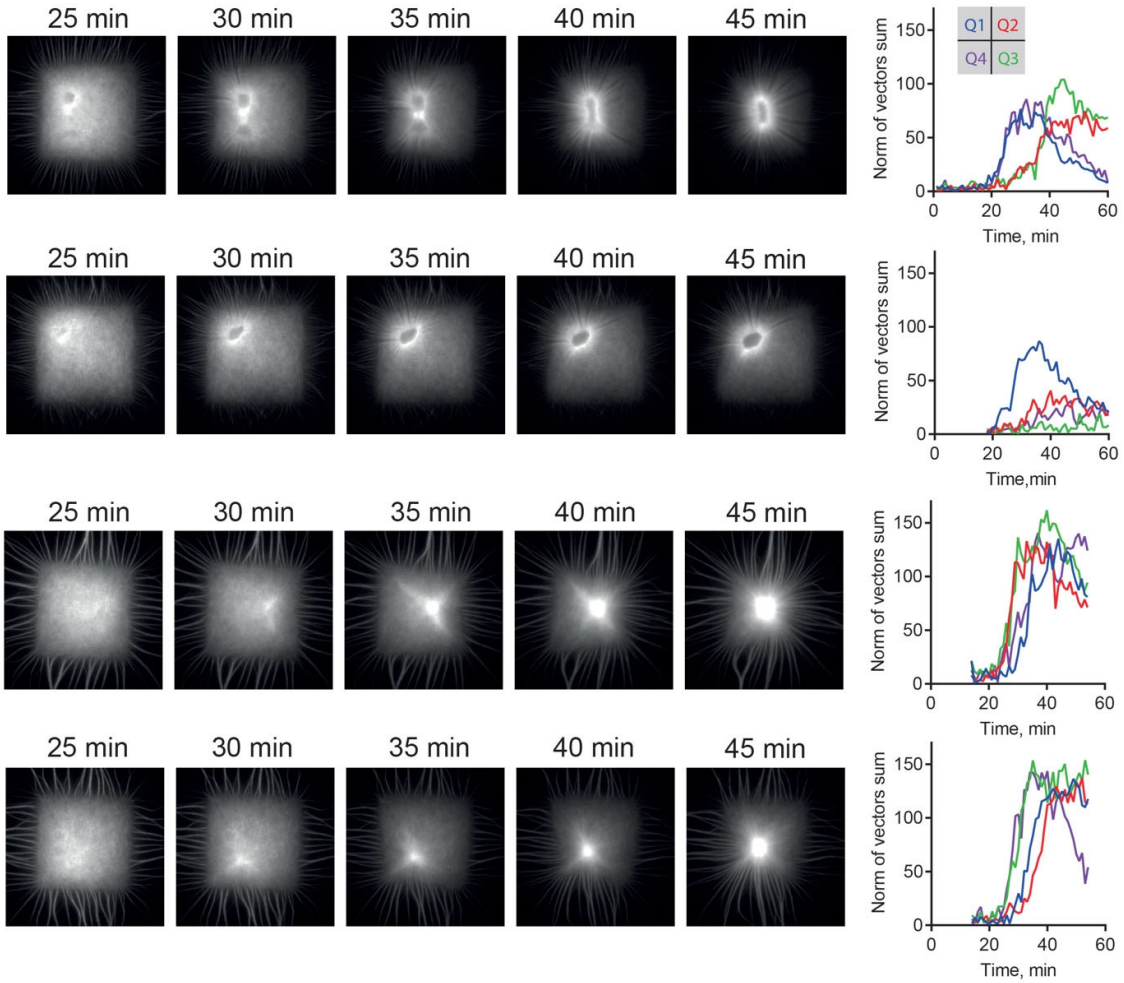

Supporting Figure 6. Actin flux is heterogeneous and asymmetric on glass micropatterns. Four examples of actin networks grown on glass substrate with the resultant of vector sum for each quadrant defined on the pattern as a function of time (obtained with PIV analysis).

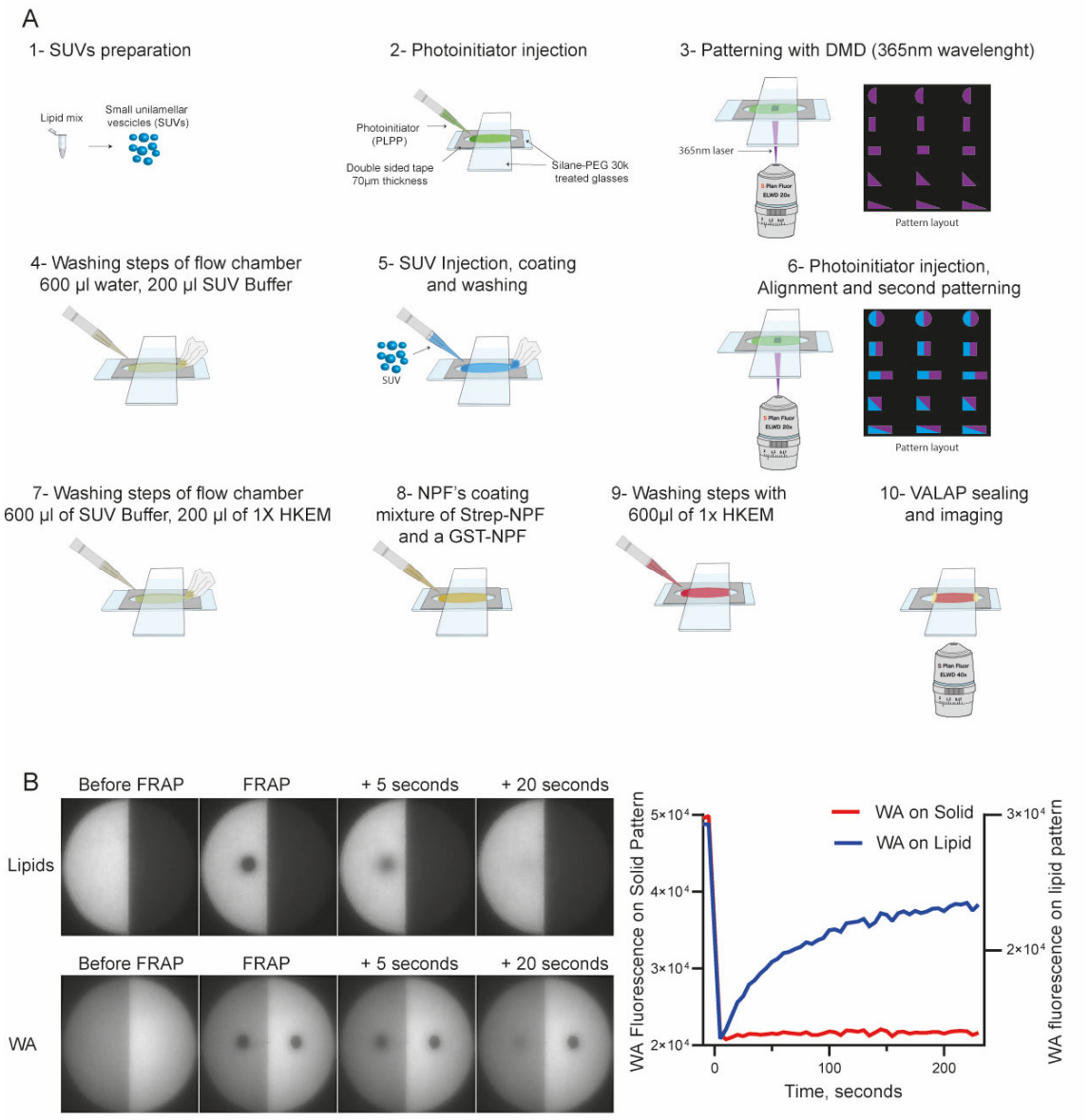

Supporting Figure 7. Heterogeneous micropatterns imposing two distinct frictions to acto-myosin networks.

A. Method to prepare heterogeneous micropatterns. **B.** Evaluation of diffusivity of lipids and NPF (WA) on heterogeneous patterns.

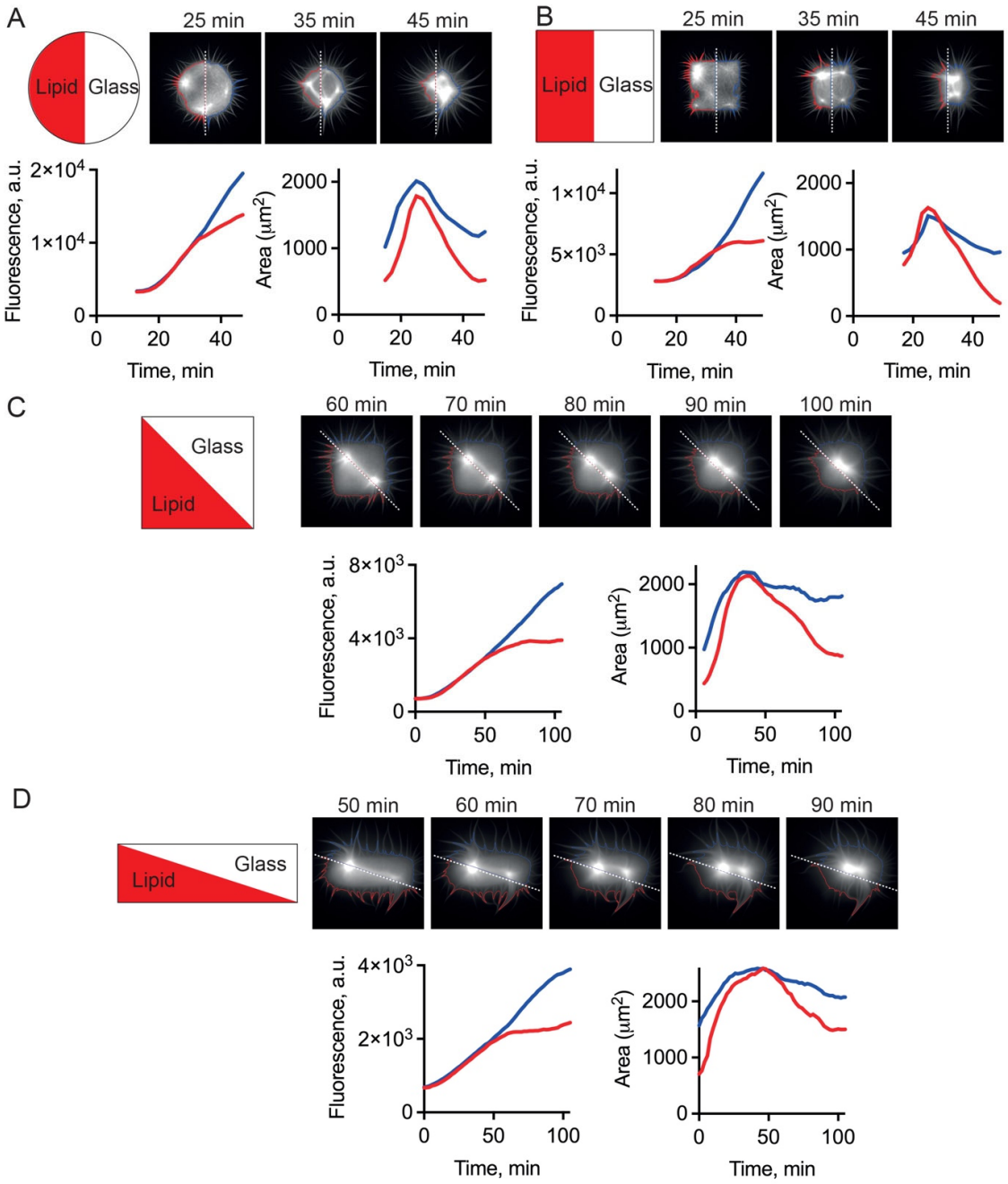

Supporting Figure 8. Kinetics of actin polymerization and contraction on heterogeneous micropatterns.

Top: Examples of snapshots of contraction on heterogeneous patterns (disc **(A)**, square **(B)**, asymmetric square **(C)**, asymmetric rectangle **(D)**). Actin network grown on lipids or glass is contoured with red or blue line respectively. Dotted white line represents the limit between the two substrates. Bottom left: Intensity of actin network grown on lipids (red) or glass (blue) for the images shown above. Bottom right: Area of actin network grown on lipids (red) or glass (blue) for the images shown above.

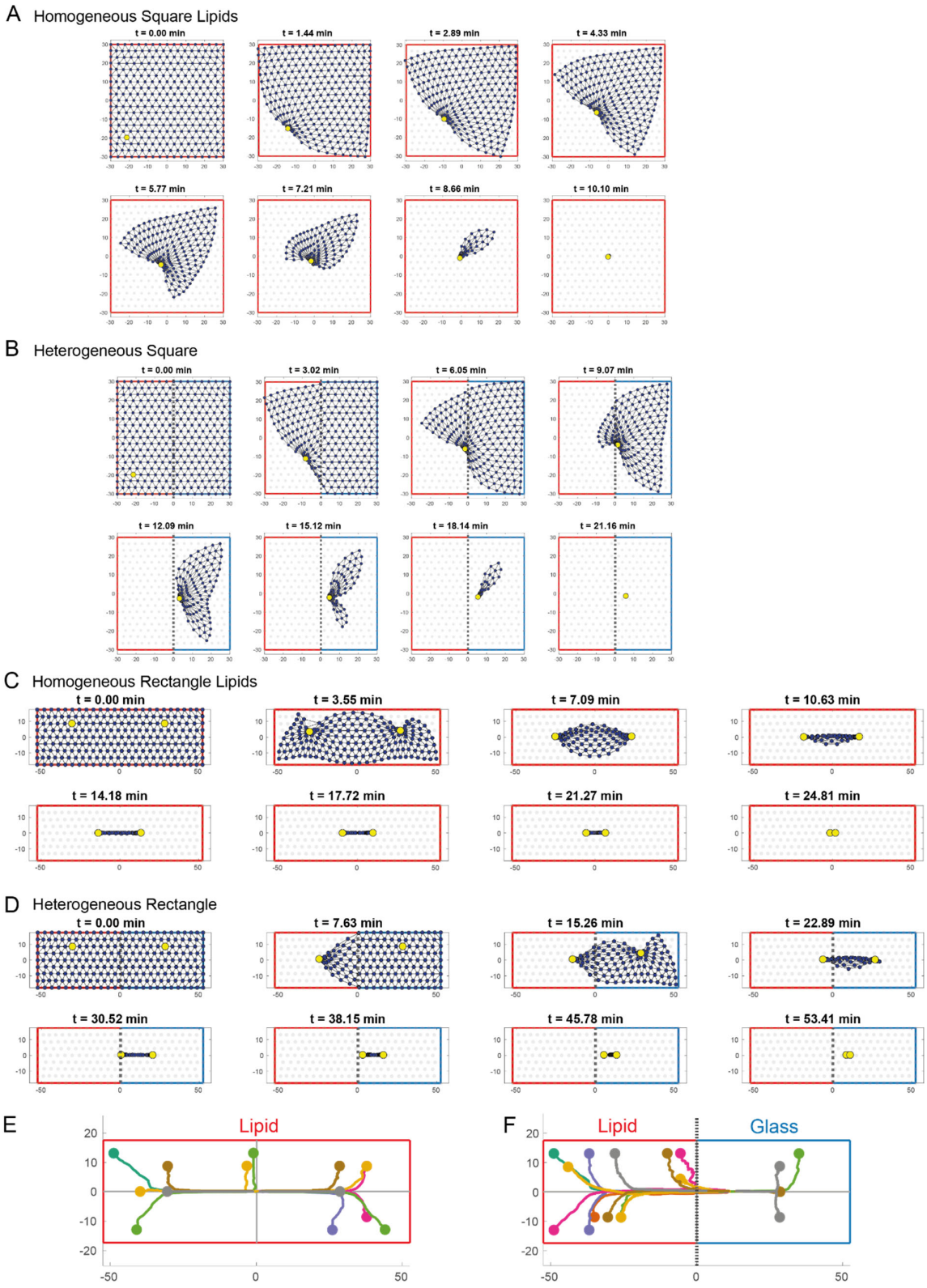

Supporting Figure 9. Additional simulations with distinct myosin distribution.
A. Example of deformation map predicted by the model for an actin network polymerized on a square lipid micropattern (asymmetric initial myosin distribution). **B.** Example of deformation map predicted by the model for an actin network polymerized on a heterogeneous square

micropattern (asymmetric initial myosin distribution). **C.** Example of deformation map predicted by the model for an actin network polymerized on a rectangular lipid micropattern (symmetric initial myosin distribution). **D.** Same as (C) on an heterogenous glass/lipid pattern. **E, F.** Predictions of myosin trajectories for an actin network contracting on a homogeneous (E) or heterogeneous (F) rectangular micropattern.

Movies Legends

Movie 1 (related to Figure 1B). Branched actin assembly on lipid micropattern
TIRF imaging of branched actin network assembly on lipid micropattern. Data is also shown in Figure 1B. Area of the zoom is 41μm². 1 image was taken every 5 seconds during 30 minutes. The movie was compressed in JPEG at 45 frames per seconds.

Movie 2 (related to Figure 1C). Characterization of the diffusion property of the lipid micropattern.
TIRF imaging before and after FRAP (zone diameter: 10μm) on lipids, NPF (WA) and Actin (after network polymerization). Data is also shown in Figure 1C. Movie duration is 25 seconds. Movie playback is 25 frames per second.

Movie 3 (related to Figure 1D). Comparison of the efficiency of actin network growth on lipid versus glass micropatterns.
TIRF imaging of branched actin assembly on lipid and glass disc micropatterns. Data is also shown in Figure 1D. 1 image was taken every 20 seconds during 40 minutes. The movie was compressed in JPEG at 20 frames per second.

Movie 4 (related to Figure 2A). Examples of contraction of disk-shaped actin networks on glass or lipid micropatterns. 4 examples of TIRF imaging of actin network contraction on a glass or lipid disc (diameter 68 μm) micropattern. 1 image was taken every 2 minutes during 45 minutes. The movie was compressed in JPEG at 10 frames per second.

Movie 5 (related to Figure 2B). Examples of contraction of square-shaped actin networks on glass or lipid micropatterns. Four examples of TIRF imaging of actin network contraction on a glass or lipid square (length 60 μm) micropattern. 1 image was taken every 2 minutes during 45 minutes. The movie was compressed in JPEG at 10 frames per second.

Movie 6 (related to Figure 3D, Glass). Examples of contraction of square-shaped actin networks on glass micropatterns.
Four examples of TIRF imaging of actin network contraction on a glass square (length 60 μm) micropattern. Actin is in red and myosin VI in green. The borders and the medians of the square are drawn in yellow. 1 image was taken every minute during 100 minutes. The movie was compressed in JPEG at 15 frames per second.

Movie 7 (related to Figure 3D, Lipids). Examples of contraction of square-shaped actin networks on lipid micropatterns.
Four examples of TIRF imaging of actin network contraction on a lipid square (length 60 μm) micropattern. Actin is in red and myosin VI in green. The borders and the medians of the square are drawn in yellow. 1 image was taken every minute during 30 minutes. The movie was compressed in JPEG at 5 frames per second.

Movie 8. Examples of contraction of full-disc shaped actin networks on lipid micropatterns.
Eight examples of time-lapse imaging of actin network contraction on a lipid full disc. Actin is in red, myosin VI is in green and lipid pattern is in blue. 1 image was taken every 2 minutes for 80 minutes. The movie was compressed in JPEG at 10 frames per second.

Movie 9. Examples of contraction of disc shaped actin networks on heterogeneous micropatterns.
Eight examples of time-lapse imaging of actin network contraction on a heterogeneous disc. Actin is in red, myosin VI is in green and lipid pattern is in blue. 1 image was taken every 2 minutes for 96 minutes. The movie was compressed in JPEG at 10 frames per second.

Movie 10. Examples of contraction of full-square shaped actin networks on lipid micropatterns.
Eight examples of time-lapse imaging of actin network contraction on a lipid full square. Actin is in red, myosin VI is in green and lipid pattern is in blue. 1 image was taken every 2 minutes. The movie was compressed in JPEG at 10 frames per second.

Movie 11. Examples of contraction of square shaped actin networks on heterogeneous micropatterns.
Eight examples of time-lapse imaging of actin network contraction on a heterogeneous square. Actin is in red, myosin VI is in green and lipid pattern is in blue. 1 image was taken every 2 minutes for 96 minutes. The movie was compressed in JPEG at 10 frames per second.

Movie 12. Examples of contraction of square shaped actin networks on diagonal heterogeneous micropatterns.
Eight examples of time-lapse imaging of actin network contraction on a diagonal heterogeneous square. Actin is in red, myosin VI is in green and lipid pattern is in blue. 1 image was taken every 2 minutes for 138 minutes. The movie was compressed in JPEG at 10 frames per second.

Movie 13. Examples of contraction of full-rectangle shaped actin networks on lipid micropatterns.
Four examples of time-lapse imaging of actin network contraction on a lipid full rectangle. Actin is in red, myosin VI is in green and lipid pattern is in blue. 1 image was taken every 2 minutes for 138 minutes. The movie was compressed in JPEG at 10 frames per second.

Movie 14. Examples of contraction of rectangle shaped actin networks on heterogeneous micropatterns.
Eight examples of time-lapse imaging of actin network contraction on a heterogeneous rectangle. Actin is in red, myosin VI is in green and lipid pattern is in blue. 1 image was taken every 2 minutes for 114 minutes. The movie was compressed in JPEG at 10 frames per second.

Movie 15. Examples of contraction of rectangle shaped actin networks on diagonal heterogeneous micropatterns.
Eight examples of time-lapse imaging of actin network contraction on a diagonal heterogeneous rectangle. Actin is in red, myosin VI is in green and lipid pattern is in blue. 1 image was taken every 2 minutes for 170 minutes. The movie was compressed in JPEG at 10 frames per second.

Movie 16. Simulation of the contraction of square shaped actin network on lipid micropattern with a symmetric initial myosin distribution.
Simulation of actin network contraction on a lipid square micropattern with a symmetric initial myosin distribution. Myosin foci are shown in yellow and contour of the pattern in red. The movie is played at 45 frames per second.

Movie 17. Simulation of the contraction of square shaped actin network on a heterogeneous micropattern with a symmetric initial myosin distribution.
Simulation of actin network contraction on a heterogeneous square micropattern with a symmetric initial myosin distribution. Myosin foci are shown in yellow, lipid part of the pattern in red, glass part of the pattern in blue. The movie is played at 85 frames per second.

Movie 18. Simulation of the contraction of square shaped actin network on lipid micropattern with an asymmetric initial myosin distribution.
Simulation of actin network contraction on a lipid square micropattern with an asymmetric initial myosin distribution. Myosin foci are shown in yellow and contour of the pattern in red. The movie is played at 20 frames per second.

Movie 19. Simulation of the contraction of square shaped actin network on a heterogeneous micropattern with an asymmetric initial myosin distribution.
Simulation of actin network contraction on a heterogeneous square micropattern with an asymmetric initial myosin distribution. Myosin foci are shown in yellow, lipid part of the pattern in red, glass part of the pattern in blue. The movie is played at 40 frames per second.

Supporting References

1. O. Lieleg, K. M. Schmoller, M. M. A. E. Claessens, A. R. Bausch, Cytoskeletal polymer networks: Viscoelastic properties are determined by the microscopic interaction potential of cross-links. *Biophys. J.* **96**, 4725–4732 (2009).
2. O. Maxian, R. P. Peláez, A. Mogilner, A. Donev, *Simulations of dynamically cross-linked actin networks: Morphology, rheology, and hydrodynamic interactions* (2021).
3. W. Strychalski, C. A. Copos, O. L. Lewis, R. D. Guy, A poroelastic immersed boundary method with applications to cell biology. *J. Comput. Phys.* **282**, 77–97 (2015).
4. R. Paul, P. Heil, J. P. Spatz, U. S. Schwarz, Propagation of mechanical stress through the actin cytoskeleton toward focal adhesions: Model and experiment. *Biophys. J.* **94**, 1470–1482 (2008).
5. P.-O. Persson, G. Strang, A Simple Mesh Generator in MATLAB. *SIAM Rev.* **46**, 329–345 (2004).
6. M. Nickaeen, *et al.*, A free-boundary model of a motile cell explains turning behavior. *PLoS Comput. Biol.* **13**, 1–22 (2017).